

DENSE CORES AND MOLECULAR OUTFLOWS IN THE OMC-2/3 REGION

YOSHIYUKI Aso,^{1,2,3} KEN'ICHI TATEMATSU,^{2,4} YUTARO SEKIMOTO,^{2,5} TAKENORI NAKANO,^{2,6} TOMOFUMI UMEMOTO,⁷
 KATSUJI KOYAMA,⁸ AND SATOSHI YAMAMOTO⁵

Received 2000 April 1; accepted 2000 June 7

ABSTRACT

We have observed the OMC-2/3 region in the $\text{H}^{13}\text{CO}^+(1-0)$, $\text{HCO}^+(1-0)$, and $\text{CO}(1-0)$ lines by using the Nobeyama 45 m radio telescope. We have identified 18 dense cores in H^{13}CO^+ and eight molecular outflows in CO and HCO^+ in OMC-2/3. Four of these outflows are newly found. The line widths of the H^{13}CO^+ cores in OMC-2/3 are twice as large as those in dark clouds, and the momentum fluxes ($\dot{P}_{\text{flow}} = P_{\text{flow}}/\tau_D = \dot{M}_{\text{flow}} V_{\text{flow}}$) of the outflows in OMC-2/3 are approximately 2 orders of magnitude larger than those of outflows in dark clouds. We found that the mass-loss rate of the outflow is proportional to the third power of the core velocity dispersion, which suggests that the outflow mass-loss rate is proportional to the mass infall rate onto the protostar. From a comparison between the properties of cores associated with protostars and those without protostars, we suggest that the dissipation of turbulence initiates star formation.

Subject headings: ISM: clouds — ISM: individual (OMC-2, OMC-3) — ISM: jets and outflows — ISM: molecules — radio lines: ISM — stars: formation

1. INTRODUCTION

The OMC-2/3 region is located at the northern end of the Orion A giant molecular cloud and is an active intermediate-mass star-forming region (Chini et al. 1997). In OMC-2, young stars, whose masses range up to $\sim 3 M_{\odot}$ (Johnson et al. 1990), form in a cluster. We selected this region because various data on star formation are available. Dense cores of this region were studied by Tatematsu et al. (1993), Cesaroni & Wilson (1994), Castets & Langer (1995), and Wilson et al. (1999). From the rotation temperature of NH_3 , Cesaroni & Wilson (1994) estimated the gas kinetic temperature of dense cores in the OMC-2/3 region to be ~ 20 K, which is higher than the typical value 10 K for cores in dark clouds (e.g., Benson & Myers 1980). New observations with bolometer arrays enable us to identify protostars (and their candidates). By observing the 1.3 mm dust continuum emission at high angular resolution ($11''$ corresponding to 0.024 pc at a distance of 450 pc), Chini et al. (1997) detected 21 pointlike sources, which can be protostars or young stellar objects (YSOs). Prior to this study, only four IRAS point sources were known as YSOs. Lis et al. (1998) identified 33 continuum sources at 350 μm , and Johnstone & Bally (1999) observed dust continuum sources at 450 and 850 μm . Reipurth, Rodriguez, & Chini (1999) made a survey at 3.6 cm with the Very Large Array (VLA) of the National Radio Observatory and detected 11 sources which are thought to be either protostars or YSOs. Yu,

Bally, & Devine (1997) discovered collimated jets from YSOs in the 2.12 μm $\text{H}_2 v = 1-0$ S(1) line. About half of the 1.3 mm dust condensations found by Chini et al. (1997) are accompanied by H_2 jets. Several outflows in OMC-2/3 have been previously reported: Fischer et al. (1985) observed the outflow associated with OMC-2, Castets & Langer (1995) detected high-velocity wing emission toward OMC-3, and Chini et al. (1997) investigated the whole OMC-2/3 region in CO(2–1) to study outflows. Tsuboi et al. (2000, in preparation) studied the X-ray emission from protostars/YSOs by using the *Chandra X-Ray Observatory*. Because the detailed information of protostars/YSOs is available for OMC-2/3, it is worthwhile investigating the relation among protostars/YSOs, dense cores, and molecular outflows in this region. We carried out new high-angular resolution observations with the Nobeyama 45 m radio telescope to search for dense cores and molecular outflows.

It has been pointed out that a dark cloud (total cloud mass $\sim 10^3 M_{\odot}$) forms only low-mass stars ($\lesssim 1 M_{\odot}$), whereas a giant molecular cloud (GMC; total cloud mass $\sim 10^5 M_{\odot}$) has a potential of forming massive to intermediate-mass stars ($> 1 M_{\odot}$; e.g., Larson 1982). To understand this difference, we compare GMCs and dark clouds regarding the properties of dense cores and regarding the properties of molecular outflows. Although dense cores in dark clouds have been extensively studied, the observational studies of dense cores in GMC are limited in number.

We used the $\text{H}^{13}\text{CO}^+(1-0)$ line to study dense cores. This line is sensitive to high-density gas ($\sim 10^5\text{--}10^6 \text{ cm}^{-3}$), which is very likely to be related to star formation, and is usually optically thin. In the Taurus low-mass star-forming region, Mizuno et al. (1994) observed dense cores in the same line at a spacing grid of $30''$ or $15''$ (corresponding to 0.02 or 0.01 pc, respectively, at a distance of 140 pc) with a $20''$ (0.14 pc) beam. For massive star-forming regions, there have been no systematic observations of dense cores with sufficient linear resolution because of their larger distances. Even the nearest massive star-forming region, the Orion molecular cloud, is 3 times more distant (450 pc) than the Taurus molecular cloud (140 pc). We searched for dense cores in

¹ Postal address: Department of Astronomy, University of Tokyo, Hongo, Tokyo 113-0033, Japan.

² Nobeyama Radio Observatory, Nobeyama, Minamisaku, Nagano 384-1305, Japan.

³ Present address: 42-11 Kirinoki-machi, Takaoka-shi, Toyama 933-0036, Japan.

⁴ tatematsu@nro.nao.ac.jp.

⁵ Department of Physics, University of Tokyo, Hongo, Tokyo 113-0033, Japan.

⁶ Present address: Department of Physics, Kyoto University, Sakyo-ku, Kyoto 606-8502, Japan.

⁷ VSOP Project Office, National Astronomical Observatory, Mitaka, Tokyo 181-8588, Japan.

⁸ Department of Physics, Kyoto University, Sakyo-ku, Kyoto 606-8502, Japan.

OMC-2/3 in the Orion molecular cloud at high angular resolution (18" or 0.039 pc).

2. OBSERVATIONS

All observations were carried out with the Nobeyama 45 m telescope during 1997 April 21–27 and 1998 March 23–25. The observational parameters are summarized in Table 1. For the receiver front end, we used the four-element focal plane SIS receiver "S115Q" (Sunada et al. 1995) to observe CO(1–0) (115 GHz) and used two SIS receivers, "S80" and "S100," to observe HCO⁺(1–0) (89 GHz) and H¹³CO⁺(1–0) (87 GHz) simultaneously. For the back end, we used high-resolution AOSs (acousto-optical spectrometers) and wideband AOSs. The high-resolution and wideband AOSs have a spectral resolution of 37 and 250 kHz, respectively. The rms noise level was 0.15, 0.08, and 0.2 K for H¹³CO⁺, HCO⁺, and CO, respectively, at the velocity resolutions listed in Table 1. The telescope pointing was calibrated by observing Orion KL in 43 GHz SiO(1–0) every 1–2 hr to be accurate to less than 5". The intensity was calibrated by the standard chopper wheel method. Furthermore, we observed Orion KL in each line at least once every day and scaled the intensity to compensate for the daily variation. The main-beam efficiencies η_{MB} at 110 and 86 GHz were 0.48 ± 0.05 and 0.49 ± 0.04 , respectively.

3. RESULTS

3.1. Dense Cores

Dense cores are identified from the H¹³CO⁺ data. The distribution of the H¹³CO⁺ emission (Fig. 1) is very fila-

mentary and is similar to that of the continuum emission (Fig. 2; Chini et al. 1997; see also Lis et al. 1998; Johnstone & Bally 1999). The H¹³CO⁺ map contains more than a dozen condensations, some of which may represent the distribution of warm dust heated by embedded protostars/YSOs.

We identify dense cores by adopting a 7σ ($1\sigma = 0.12$ K km s⁻¹) level of the integrated intensity as the threshold. We regard two maxima as different cores if the "valley" between them is deeper than 2σ . We use the velocity information to separate cores which overlap with each other along the line of sight. A total of 18 dense cores are identified (Table 2).

We classify the core as being associated with a protostar/YSO if both of the following conditions are satisfied: (1) a 1.3 mm continuum source (Chini et al. 1997) or a 350 μ m continuum source (Lis et al. 1998) is located within the half-intensity contour and (2) an H₂ jet (Yu et al. 1997) or a molecular outflow (this study) is associated with the core. With this criterion, 10 of the 18 cores are classified as accompanying protostars/YSOs.

The physical parameters of dense cores are derived in the following way. The radius R is defined as $R = [(A/\pi) - (\text{HPBW}/2)^2]^{1/2}$, which is corrected for spatial broadening due to the telescope beam. Here A is the area within the half-intensity contour of the integrated intensity. Figure 3 shows examples of H¹³CO⁺ spectra. The antenna temperature T_A^* is derived from Gaussian fitting to the line profile at a local integrated intensity maximum. The line width ΔV_{obs} is an average value within the half-intensity

TABLE 1
OBSERVATIONAL PARAMETERS

Line	Half-Power Beam Width (HPBW) (arcsec)	Spacing Grid (arcsec)	Velocity Resolution (km s ⁻¹)
CO(1–0)	15 (0.033 pc)	34 (0.074 pc)	0.65
HCO ⁺ (1–0)	18 (0.039 pc)	34 (0.074 pc)	0.83
H ¹³ CO ⁺ (1–0)	18 (0.039 pc)	17 (0.037 pc) or 34 (0.074 pc)	0.13

TABLE 2
THE H¹³CO⁺ CORES IN THE OMC-2/3 REGION (1)

Core Name	R.A. (1950)	Decl. (1950)	V_{LSR} (km s ⁻¹)	R (pc)	T_A^* (K)	ΔV_{obs} (km s ⁻¹)
AC1	5 32 45.9	−5 01 26	11.4	0.052	2.1	0.95
AC2	5 32 48.1	−5 01 60	11.2	0.057	1.7	0.98
AC3	5 32 50.4	−5 02 34	11.2	0.067	2.8	0.99
AC4	5 32 56.1	−5 03 08	11.2	0.061	1.5	0.98
AC5	5 32 59.5	−5 03 08	11.4	0.057	1.1	0.98
AC6	5 32 50.4	−5 04 25	10.5	0.072	1.7	0.95
AC7	5 32 57.2	−5 04 33	11.0	0.052	1.6	0.81
AC8	5 32 57.9	−5 05 24	11.1	0.078	1.7	0.89
AC9	5 32 52.7	−5 07 06	11.3	0.052	1.7	1.03
AC10	5 32 59.5	−5 07 23	11.4	0.081	2.3	0.74
AC11	5 32 57.2	−5 07 57	11.5	0.047	1.2	0.93
AC12	5 33 04.1	−5 07 57	11.8	0.081	1.0	0.86
AC13	5 33 00.7	−5 09 05	11.6	0.047	1.1	1.07
AC14	5 32 56.1	−5 09 22	11.8	0.084	1.4	1.15
AC15	5 32 57.2	−5 10 13	11.2	0.092	1.0	1.10
AC16	5 32 53.8	−5 11 55	11.5	0.047	0.8	0.81
AC17	5 32 59.5	−5 11 55	11.3	0.100	1.4	1.07
AC18	5 33 02.9	−5 11 55	11.1	0.061	0.8	0.88

NOTE.—Units of right ascension are hours, minutes, and seconds, and units of declination are degrees, arcminutes, and arcseconds.

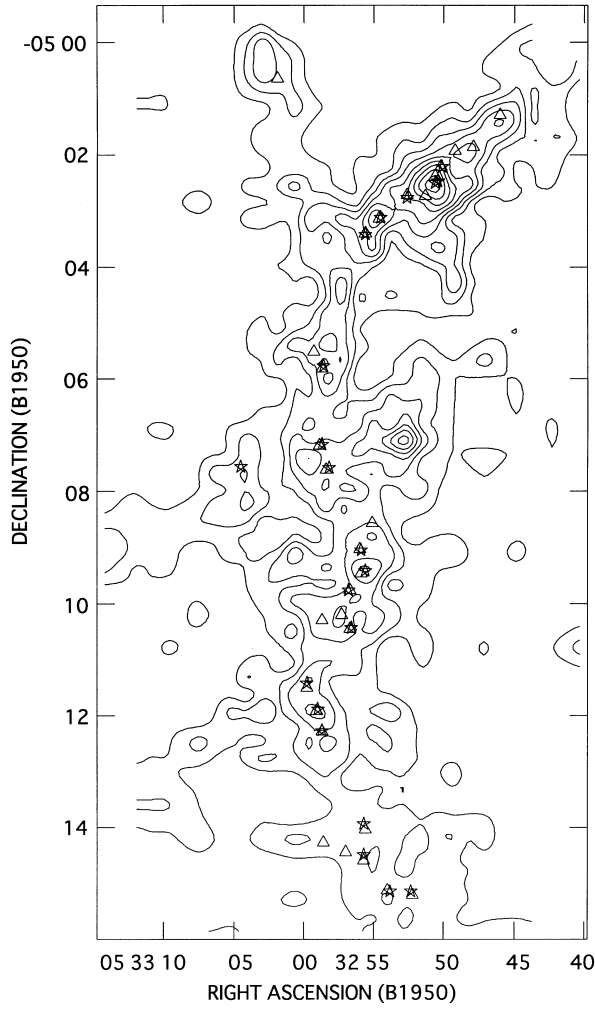


FIG. 1.— $\text{H}^{13}\text{CO}^+(1-0)$ integrated intensity map of the OMC-2/3 region. Contour intervals are 0.36 K km s^{-1} starting at 0.36 K km s^{-1} . The stars mark the 1.3 mm continuum sources (Chini et al. 1997), and the triangles mark the $350 \mu\text{m}$ continuum sources (Lis et al. 1998).

contour of the integrated intensity. We derive the column density assuming local thermodynamic equilibrium (LTE) and optically thin emission. We use a formula, $N_{\text{tot}} = (3k/4\pi^3 \mu^2 \nu)(kT_{\text{ex}}/h\nu) \exp(h\nu/T_{\text{ex}}) \int T_R dv$ (cm^{-2}), where N_{tot} is the column density of the molecule at all energy levels. The radiation temperature T_R is defined as $T_R = T_A^*/\eta_{\text{MB}}$. For the $\text{H}^{13}\text{CO}^+(1-0)$ line, we have $N(\text{H}_2) = 1.0 \times 10^{21} T_{\text{ex}} \exp(4.16/T_{\text{ex}}) \int T_R dv$ (cm^{-2}), by adopting an abundance ratio of $[\text{HCO}^+]/[\text{H}_2] = 4.0 \times 10^{-9}$ (Lee, Bettens, & Herbst 1996), and a terrestrial ratio of $\text{C}/^{13}\text{C} = 89$. The LTE mass is defined as $M_{\text{core}} = N(\text{H}_2) A m_{\text{H}} \mu$, where m_{H} is the hydrogen mass and μ is the mean molecular weight per H atom (2.8). The virial mass is defined as

$$M_{\text{vir}}(M_{\odot}) = 209 R(\text{pc}) \Delta V_{\text{tot}}(\text{km s}^{-1})^2 \quad (1)$$

(e.g., MacLaren, Richardson, & Wolfendale 1988). The total line width ΔV_{tot} is given by

$$\Delta V_{\text{tot}} = \left[\Delta V_{\text{obs}}^2 + 8 \ln 2 k T_k \left(\frac{1}{m} - \frac{1}{m_{\text{obs}}} \right) \right]^{1/2}, \quad (2)$$

where m , m_{obs} , and T_k are the mean mass of the molecule (2.33 amu), the mass of the observed molecule, and the kinetic temperature of the gas, respectively. We adopt the

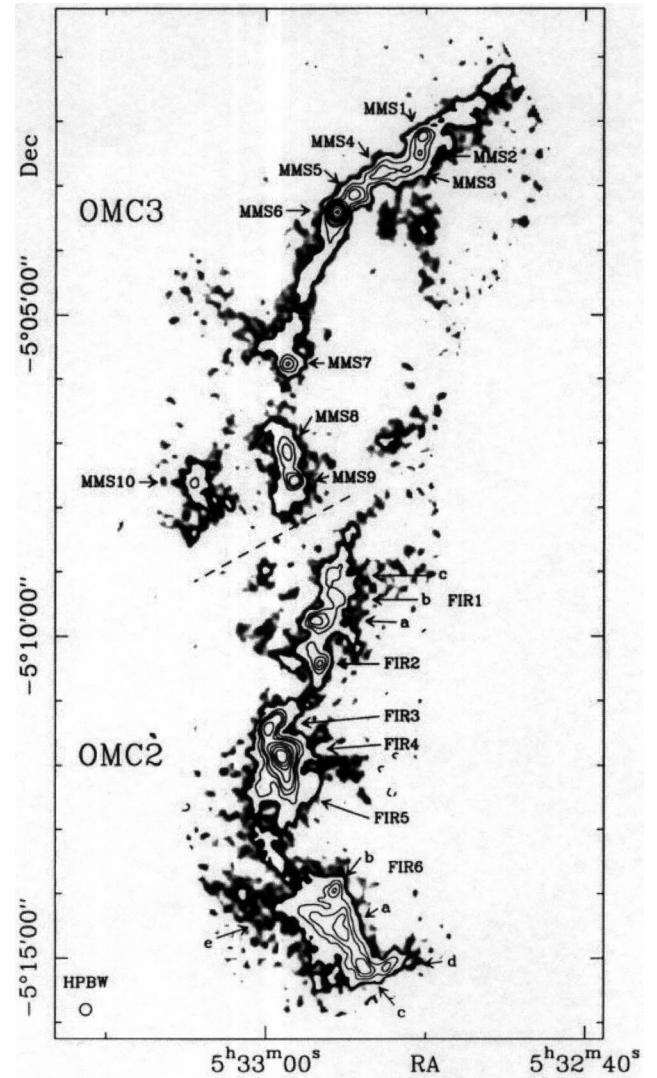


FIG. 2.—A 1.3 mm map at the OMC-2/3 region reproduced from Chini et al. (1997).

NH_3 rotation temperature measured by Cesaroni & Wilson (1994) as T_k . The derived physical parameters are listed in Tables 2 and 3.

3.2. Molecular Outflows

We searched for the high-velocity wing emission in CO and HCO^+ . We identified blue and red lobes associated with continuum sources as outflows (Figs. 4 and 5). We take into account the axis of the H_2 jet to determine with which protostar/YSO the high-velocity emission is associated. Eight outflows are identified (Tables 4–7). Individual outflows are discussed in the Appendix. Four of them are clearly separated: MMS 7, MMS 9, FIR 1 (1.3 mm continuum sources by Chini et al. 1997), and OMC-2. The others are more or less confused: CSO 2 ($350 \mu\text{m}$ continuum source by Lis et al. 1998), MMS 2–4, MMS 5, and MMS 10 (1.3 mm continuum sources by Chini et al. 1997). Four outflows associated with MMS 5 (or MMS 6), MMS 7, MMS 9 (or MMS 8), and OMC-2 are previously known (Fischer et al. 1985; Chini et al. 1997). Four outflows associated with CSO 2, MMS 2–4, MMS 10, and FIR 1 are newly identified. Spectra of some outflows are shown in Figure 6. In OMC-2/3, at least eight outflows are crowded with a

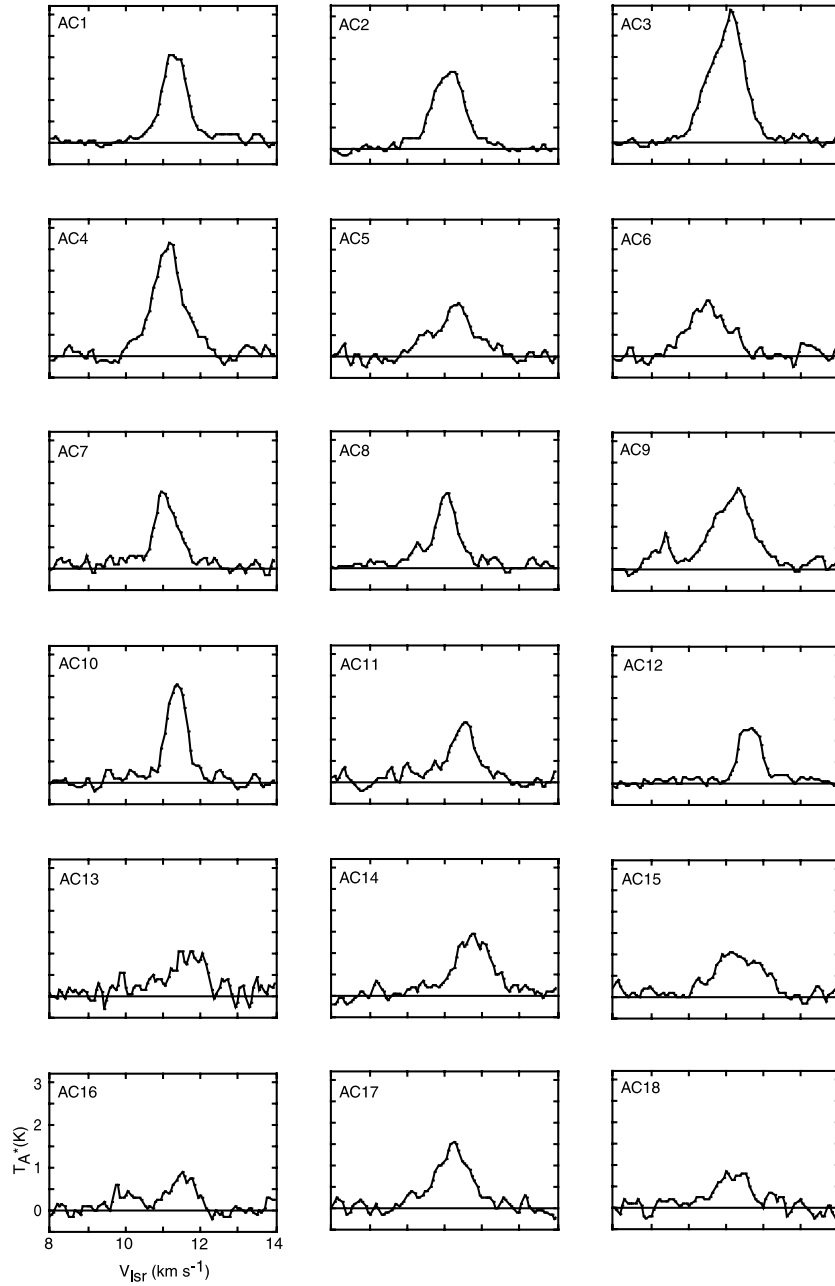


FIG. 3.— H^{13}CO^+ line profiles toward the peaks of 18 dense cores

mean separation of about 0.2 pc, which is much smaller than the average separation of 5 pc in Orion A and S287 reported by Fukui et al. (1993). This fact suggests that the OMC-2/3 region is an exceptionally active star formation site. In the region south of OMC-2, we cannot separate outflows because these overlap.

The line parameters of the outflow are derived by using the spectrum averaged over each lobe of the outflow; V_{mean} is the intensity-weighted mean velocity, V_{max} is the maximum velocity extent measured from the systemic velocity at the zero level, R_{max} is the maximum extent of the 3σ contour measured from the source, and the dynamical timescale τ_D is defined as $\tau_D = R_{\text{max}}/V_{\text{max}}$. We estimate the column density assuming LTE and optically thin emission. We assume the excitation temperature to be $T_{\text{ex}} = 20$ K and adopt abundance ratios, $[\text{CO}]/[\text{H}_2] = 1 \times 10^{-4}$ and

$[\text{HCO}^+]/[\text{H}_2] = 4.0 \times 10^{-9}$. Then we have $N(\text{H}_2) = 7.3 \times 10^{18} \int T_R dv \text{ (cm}^{-2}\text{)}$ for the $\text{CO}(J=1-0)$ line, and $N(\text{H}_2) = 2.7 \times 10^{20} \int T_R dv \text{ (cm}^{-2}\text{)}$ for the $\text{HCO}^+(J=1-0)$ line. These equations give lower limits to the column density because the lines might be optically thick. The outflow mass and momentum are defined by $M_{\text{flow}} = N(\text{H}_2) A m_{\text{H}} \mu$ and $P_{\text{flow}} = M_{\text{flow}} V_{\text{mean}}$, respectively. The mass-loss rate and the momentum flux are defined by $\dot{M}_{\text{flow}} = M_{\text{flow}}/\tau_D$ and $\dot{P}_{\text{flow}} = P_{\text{flow}}/\tau_D$, respectively, where M_{flow} and P_{flow} are the total (blue and red lobes) outflow mass and the total momentum, respectively.

3.3. Column Density

It is likely that OMC-3 is in younger evolutionary stage than OMC-2 because pointlike dust continuum sources in OMC-3 show a colder color (Chini et al. 1997). According

TABLE 3
THE H^{13}CO^+ CORES IN THE OMC-2/3 REGION (2)

Core Name	M_{core} (M_{\odot})	M_{vir} (M_{\odot})	T_k^a (K)	Continuum Sources ^b	H_2 Jets and Molecular Outflows ^c	CS Cores ^d
AC1	12.5	13.3	19	350	O	3
AC2	16.8	15.3	19	350	(H)	3
AC3	30.8	18.6	19	350, 1.3	H, O	3
AC4	21.2	16.4	19	350, 1.3	H, O	4
AC5	11.5	15.2	(19)			4
AC6	18.0	18.5	(19)			6
AC7	10.8	10.9	(19)			5
AC8	17.1	17.9	18	350, 1.3	H, O	5
AC9	16.0	14.9	(18)			6
AC10	21.7	14.4	18	350, 1.3	H, O	
AC11	8.9	11.7	18			
AC12	17.2	17.7	(18)	1.3	O	7
AC13	9.4	15.2	(23)			
AC14	29.3	30.1	23	350, 1.3	H, O	8
AC15	34.8	31.1	23	350, 1.3	H	8
AC16	6.3	10.6	24			
AC17	34.8	32.8	24	350, 1.3	H, O	11
AC18	9.5	15.1	24			11

^a Cesaroni & Wilson 1994.

^b “350” and “1.3” mean that 350 μm (Lis et al. 1998) and 1.3 mm (Chini et al. 1997) continuum pointlike sources are associated, respectively.

^c “H” and “O” mean that H_2 jets (Yu et al. 1997) and molecular outflows (this work) are associated, respectively.

^d Tatematsu et al. 1993.

to the criterion of André, Ward-Thompson, & Barsony (1993), six sources in OMC-3 are Class 0 protostars, having $L_{\text{bol}}/L_{\text{mm}} < 200$ (Chini et al. 1997). More evolved emission-line stars are distributed in the OMC-2 region (Chini et al. 1997; Herbig & Bell 1988).

Figure 7 shows the map of the integrated intensity ratio of H^{13}CO^+ to HCO^+ . The ratio is higher in OMC-3 than in OMC-2, which means the optical depth of H^{13}CO^+ in OMC-3 is larger than that in OMC-2. We obtain $\tau(\text{H}^{13}\text{CO}^+) \sim 0.4$ and ~ 0.1 for OMC-3 and OMC-2,

respectively. The $\text{C}^{18}\text{O}(1-0)$ integrated intensity map⁹ also suggests larger column density in the OMC-3 region (Fig. 8; Hirano et al. 2000, in preparation). It seems that the OMC-3 region retains more molecular gas, while the gas has been partly dispersed in OMC-2 probably due to the activities of protostars/YSOs.

⁹ The data of the Nobeyama 45 m Radio Telescope used in this paper were obtained from the data archive of the Nobeyama Radio Observatory (<http://nrodb.nro.nao.ac.jp>).

TABLE 4
PARAMETERS OF THE CO OUTFLOWS (1)

Source	Lobe	Velocity Range (km s^{-1})	R_{max} (pc)	V_{max} (km s^{-1})	V_{mean} (km s^{-1})	τ_D (10^4 yr)	M_{flow} (M_{\odot})	P_{flow} ($M_{\odot} \text{ km s}^{-1}$)
CSO 2	Blue	5–7.5	0.14	6.0	3.3	2.3	0.031	0.10
	Red	13.5–17	0.10	4.1	2.0	2.4	0.059	0.12
AC3 (MMS 2–4)	Blue	–2 to 9	0.41	12.0	4.2	3.4	0.24	1.0
	Red				No			
MMS 5	Blue	4–8	0.25	7.8	4.6	3.1	0.082	0.38
	Red	13.5–18	0.18	5.9	2.8	3.0	0.065	0.18
MMS 7	Blue	–1 to 9	0.28	11.5	3.7	2.4	0.26	0.97
	Red	13.5–20	0.86	8.2	3.6	6.2	0.26	0.94
MMS 9	Blue	–2 to 7	0.50	13.5	6.6	3.6	0.38	2.5
	Red	14–23	0.35	11.5	3.8	3.0	0.36	1.4
MMS 10	Blue	0–8	0.31	9.8	4.5	3.1	0.14	0.65
	Red				Confused with MMS 9			
FIR 1	Blue	0–8	0.17	8.5	3.3	2.0	0.16	0.42
	Red	13.5–22	0.17	11.0	2.5	1.51	0.33	0.83
OMC-2	Blue	0–8.5	0.19	11.5	3.6	1.6	0.30	1.1
	Red	13.5–22	0.17	7.4	3.9	2.3	0.34	1.3

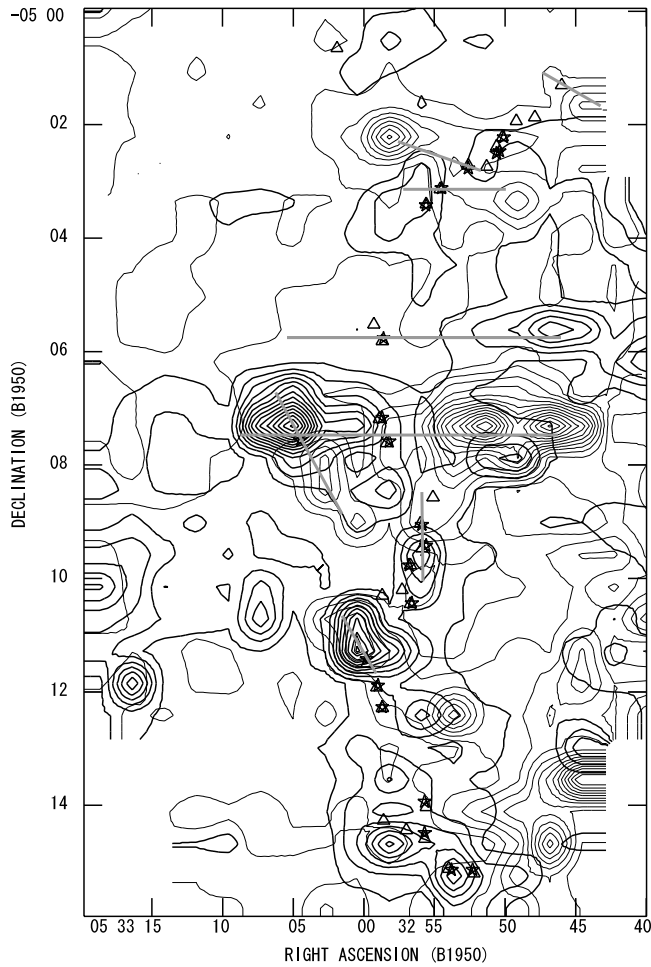


FIG. 4.—CO integrated intensity map of the OMC-2/3 region. The thin contours show the blueshifted gas ($0.5\text{--}7.5\text{ km s}^{-1}$), and the thick contours show the redshifted gas ($14\text{--}21\text{ km s}^{-1}$). Contour intervals are 1.4 K km s^{-1} starting at 1.4 K km s^{-1} . The gray lines show our identification of the outflow axes.

4. COMPARISON WITH DARK CLOUDS

4.1. Dense Cores

We compare the physical properties of the H^{13}CO^+ cores in OMC-2/3 with those in Taurus (Mizuno et al. 1994) to investigate the difference in cores between giant molecu-

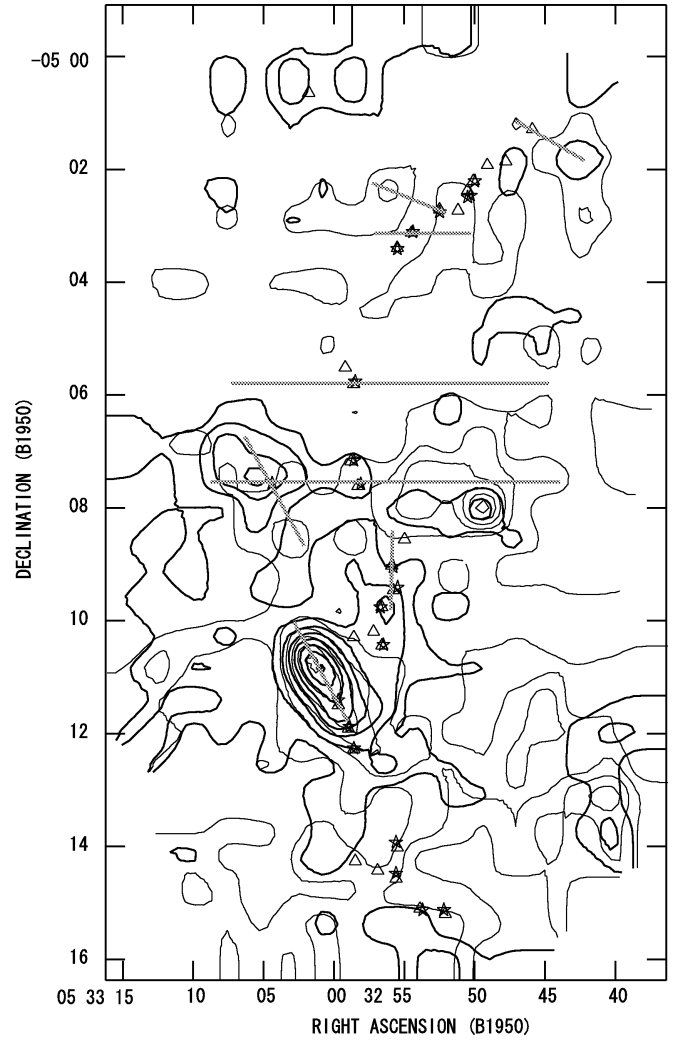


FIG. 5.— HCO^+ integrated intensity map of the OMC-2/3 region. The thin contours show the blueshifted gas ($0.5\text{--}8.5\text{ km s}^{-1}$), and the thick contours show the redshifted gas ($13\text{--}21\text{ km s}^{-1}$). Contour intervals are 0.4 K km s^{-1} starting at 0.4 K km s^{-1} . The gray lines show our identification of the outflow axes.

lar clouds and dark clouds. Figure 9 shows the line width (ΔV_{obs})-radius (R) diagram of the H^{13}CO^+ cores in the OMC-2/3 region (*circles*) and in Taurus (*triangles*) (see also Table 8). Figure 10 shows the histograms of the radius (R)

TABLE 5
PARAMETERS OF THE CO OUTFLOWS (2)

Source	\dot{M}_{flow} (M_{\odot})	\dot{P}_{flow} ($M_{\odot}\text{ km s}^{-1}$)	τ_D (10^4 yr)	\dot{M}_{flow} ($10^{-5}\text{ }M_{\odot}\text{ yr}^{-1}$)	\dot{P}_{flow} ($10^{-5}\text{ }M_{\odot}\text{ km s}^{-1}\text{ yr}^{-1}$)	L_{bol} (L_{\odot})	M_{env} (M_{\odot})
CSO 2	0.090	0.22	2.3	0.39	0.96		
AC3 (MMS 2–4).....	0.24	1.0	3.3	0.73	3.1	$<56^{a,b}$	$11^{a,b}$
MMS 5	0.15	0.56	3.0	0.49	1.9		
MMS 7	0.53	1.9	4.3	1.2	4.5	76^a	8^a
MMS 9	0.60^c	3.2^c	3.3	1.8	9.8	$<94^a$	10^a
MMS 10.....	0.29^d	1.3^d	3.1	0.93	4.2		
FIR 1	0.49	1.4	1.7	2.9	8.0	$128^{a,c}$	$5^{a,e}$
OMC-2	0.64	2.4	1.9	3.4	12.7		

^a Chini et al. 1997.

^b MMS 4 only.

^c The red lobe of MMS 10 was subtracted assuming the symmetry of the bipolar outflow of MMS 10.

^d Twice the value for the blue lobe assuming the symmetry of the bipolar outflow.

^e FIR 1c only.

TABLE 6
PARAMETERS OF THE HCO⁺ OUTFLOWS (1)

Source	Lobe	Velocity Range (km s ⁻¹)	R_{\max} (pc)	V_{\max} (km s ⁻¹)	V_{mean} (km s ⁻¹)	τ_D (10 ⁴ yr)	\dot{M}_{flow} (M_{\odot})	\dot{P}_{flow} (M_{\odot} km s ⁻¹)
CSO 2	Blue	3–8.5	0.14	8.0	3.2	1.7	0.18	0.57
	Red	13–17	0.10	5.3	2.8	1.8	0.16	0.46
AC3 (MMS 2–4)	Blue	0–9	0.17	8.8	4.1	1.9	0.14	0.58
	Red				No			
MMS 5	Blue	3–9	0.27	7.1	3.0	3.7	0.17	0.50
	Red	13–17	0.09	3.9	2.1	2.2	0.035	0.073
MMS 7	Blue	0–9	0.32	10.7	4.0	2.9	0.13	0.51
	Red	13–28	0.32	17.0	7.6	1.8	0.21	1.6
MMS 9	Blue	–5 to 9	0.27	9.6	3.4	2.8	0.81	2.8
	Red	13.5–25	0.38	11.2	4.5	3.3	0.74	3.4
MMS 10	Blue	0–10	0.27	9.6	3.4	2.8	0.47	1.6
	Red				Confused with MMS 9			
FIR 1	Blue	0–9.5	0.19	10.0	2.9	1.9	0.48	1.4
	Red	13–22	0.19	11.0	3.3	1.7	0.64	2.1
OMC-2	Blue	–10 to 9.5	0.34	20.0	5.4	1.7	1.6	8.5
	Red	13–25	0.34	14.0	5.0	2.4	2.0	9.8

TABLE 7
PARAMETERS OF THE HCO⁺ OUTFLOWS (2)

Source	\dot{M}_{flow} (M_{\odot})	\dot{P}_{flow} (M_{\odot} km s ⁻¹)	τ_D (10 ⁴ yr)	\dot{M}_{flow} (10 ⁻⁵ M_{\odot} yr ⁻¹)	\dot{P}_{flow} (10 ⁻⁵ M_{\odot} km s ⁻¹ yr ⁻¹)
CSO 2	0.34	1.0	1.8	1.9	5.7
AC3 (MMS 2–4)	0.14	0.58	1.9	0.74	3.0
MMS 5	0.20	0.57	3.0	0.67	1.9
MMS 7	0.34	2.1	2.4	1.4	8.8
MMS 9	1.1 ^a	4.5 ^a	3.0	3.6	15.1
MMS 10	0.93 ^b	3.2 ^b	2.8	3.3	11.3
FIR 1	1.1	3.5	3.6	3.1	9.8
OMC-2	3.5	8.4	2.0	17.7	41.8

^a The red lobe of MMS 10 assuming the symmetry of the bipolar outflow of MMS 10.

^b Twice the value for the blue lobe assuming the symmetry of the bipolar outflow.

and the line width (ΔV_{obs}). We find from these figures that the Orion cores systematically have larger line widths. This result is consistent with the finding of Harju, Walmsley, & Wouterloot (1991), based on the observations in NH₃ and that of Tatematsu et al. (1993) in CS. Mizuno et al. (1994) found that, in Taurus, cores with protostars/YSOs have smaller size and larger line widths than cores without protostars/YSOs. However, in OMC-2/3, there is no clear difference in line width between cores with protostars/YSOs and those without protostars/YSOs. Cores with protostars/YSOs have similar or slightly larger size than those without protostars/YSOs in OMC-2/3.

4.2. Molecular Outflows

We compare the CO outflows in OMC-2/3 with those in dark clouds observed by Bontemps et al. (1996) (Tables 9

and 10). For a fair comparison, we multiply the observed \dot{P}_{flow} for the OMC-2/3 outflows by a factor of 10 to correct for the outflow orientation and line opacity (eq. [2] of Bontemps et al. 1996). In the OMC-2/3 region, the envelope mass (M_{env}), the bolometric luminosity (L_{bol}), and the momentum flux (\dot{P}_{flow}) are all 1–2 orders of magnitude larger than those in dark clouds (Fig. 11). Bontemps et al. (1996) found that \dot{P}_{flow} is correlated with M_{env} and L_{bol} . The outflows of OMC-2/3 are located on the extended part of this correlation.

5. DISCUSSION

5.1. Relation between Line Widths of Dense Cores and Mass-Loss Rates of Outflows

We have found that the H¹³CO⁺ cores in OMC-2/3 have larger line widths ($\Delta V \sim 1$ km s⁻¹) than those in the Taurus dark cloud ($\Delta V \sim 0.5$ km s⁻¹; Mizuno et al. 1994) and also have found that the outflows in OMC-2/3 have larger momentum fluxes ($\sim 10^{-3}$ M_{\odot} km s⁻¹ yr⁻¹) than those in dark clouds ($\sim 10^{-6}$ to 10^{-4} M_{\odot} km s⁻¹ yr⁻¹; Bontemps et al. 1996). A possible interpretation for this fact is that cores with larger line widths have larger mass accretion rates onto protostars, and larger mass accretion rates cause larger momentum fluxes of outflows (Shu et al. 1988; Edwards, Ray, & Mundt 1993). Larger mass accretion rates may lead to systematically larger stellar masses in OMC-2/3 than in dark clouds.

TABLE 8
THE MEAN RADIUS AND LINE WIDTH OF THE H¹³CO⁺ CORES
IN OMC-2/3 AND TAURUS

Region	R (pc)	ΔV_{obs} (km s ⁻¹)
OMC-2/3 (without YSOs)	0.054 ± 0.009	0.92 ± 0.09
OMC-2/3 (with YSOs)	0.075 ± 0.016	0.96 ± 0.12
Taurus (without YSOs)	0.090 ± 0.038	0.48 ± 0.07
Taurus (with YSOs)	0.028 ± 0.005	0.65 ± 0.13

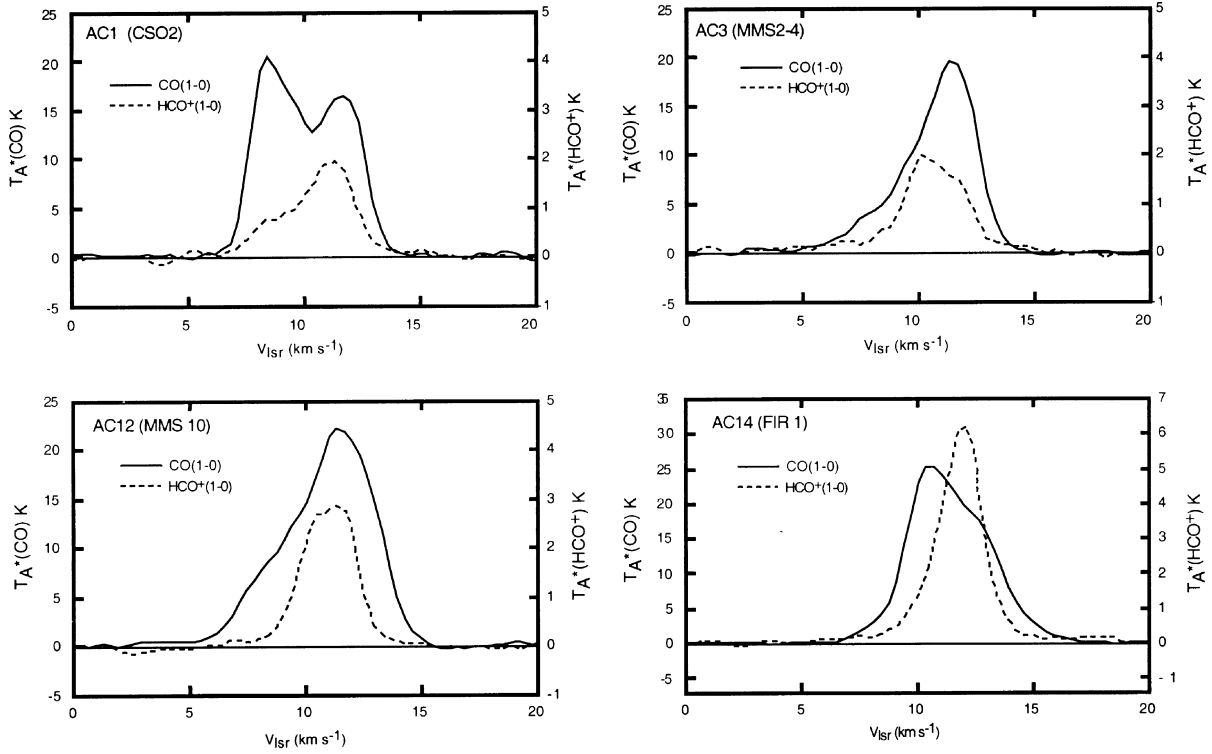


FIG. 6.—Spectra of CO(1–0) and HCO⁺(1–0) toward the outflow CSO 2 (5^h32^m44^s.7, –5°1′43″), MMS 2–4 (5^h32^m56^s.1, –5°2′17″), MMS 10 (5^h33^m2^s.9, –5°8′31″), and FIR 1 (5^h32^m56^s.1, –5°9′39″).

We investigate the correlation between the core line widths ΔV_{tot} (eq. [2]) and the mass-loss rates of outflows (\dot{M}_{flow}). In addition to our data, we use data of outflows in dark clouds (Bachiller, Martin-Pintado, & Planesas 1991; Myers et al. 1988; Myers & Benson 1983; Snell, Loren, & Plambeck 1980; Benson & Myers 1989; Goldsmith, Snell, & Heyer 1984) and those of more massive protostars, Orion S and Orion KL in the Orion A cloud (Schmid-Burgk et al. 1990; Batrla et al. 1983; Snell et al. 1984).

A theoretical study suggests that the mass accretion rate onto the protostar is $\sim C_{\text{eff}}^3/G$ (Shu 1977), where C_{eff} is the effective sound speed including turbulence (nonthermal component)

$$C_{\text{eff}} = \left(\frac{\Delta V_{\text{tot}}^2}{8 \ln 2} \right)^{1/2} = \left[\frac{\Delta V_{\text{obs}}^2}{8 \ln 2} + kT \left(\frac{1}{m} - \frac{1}{m_{\text{obs}}} \right) \right]^{1/2}. \quad (3)$$

If the mass ejection rate of outflow is proportional to the mass accretion rate (Shu et al. 1988; Edwards et al. 1993), the mass ejection rate is also proportional to the third power of effective sound speed, i.e.,

$$\dot{M}_{\text{flow}} \propto \dot{M}_{\text{acc}} \sim C_{\text{eff}}^3/G = (\Delta V_{\text{tot}}/\sqrt{8 \ln 2})^3/G. \quad (4)$$

A linear least-squares fit to the observed data leads to

$$\dot{M}_{\text{flow}} \propto (\Delta V_{\text{tot}})^{3.6 \pm 0.5}. \quad (5)$$

However, the observed line widths may be dynamically affected by outflows. In outflows in dark clouds, the line widths of cores may have been increased by outflow activities (Myers et al. 1988). For the OMC-2/3 cores, there is no clear difference in line width between cores with YSOs and those without YSOs (§ 4.1), so it seems that the outflows hardly affect the core line width.

TABLE 9
OUTFLOWS IN DARK CLOUDS, ORION S, AND ORION KL

SOURCE	\dot{M}_{flow}		ΔV_{obs}		ΔV_{tot} (km s ⁻¹)	T_k	
	10 ⁻⁶ M _⊙ yr ⁻¹	Reference	km s ⁻¹	Reference		K	Reference
IRAS 03282+3035	12	1	0.48	1	0.66	11.8	1
L1489	0.31	2	0.28	3	0.50	10	3
L1551-IRS5	5.3	4	0.51	3	0.67	11	3
B35	4.8	2	0.82	5	0.98	16.6	5
L43	0.65	2	0.40	3	0.60	12	3
L778	1.0	2	0.40	5	0.59	11.2	5
B335	1.1	6	0.40	5	0.57	9.9	5
L1172D	5.2	2	0.36	3	0.56	11	3
Orion S	100	7	2.2	8	1.1	100	8
Orion KL	5500	9	3.6	10	3.8	85	8

REFERENCES.—(1) Bachiller et al. 1991; (2) Myers et al. 1988; (3) Myers & Benson 1983; (4) Snell et al. 1980; (5) Benson & Myers 1989; (6) Goldsmith et al. 1984; (7) Schmid-Burgk et al. 1990; (8) Batrla et al. 1983; (9) Snell et al. 1984; (10) this work.

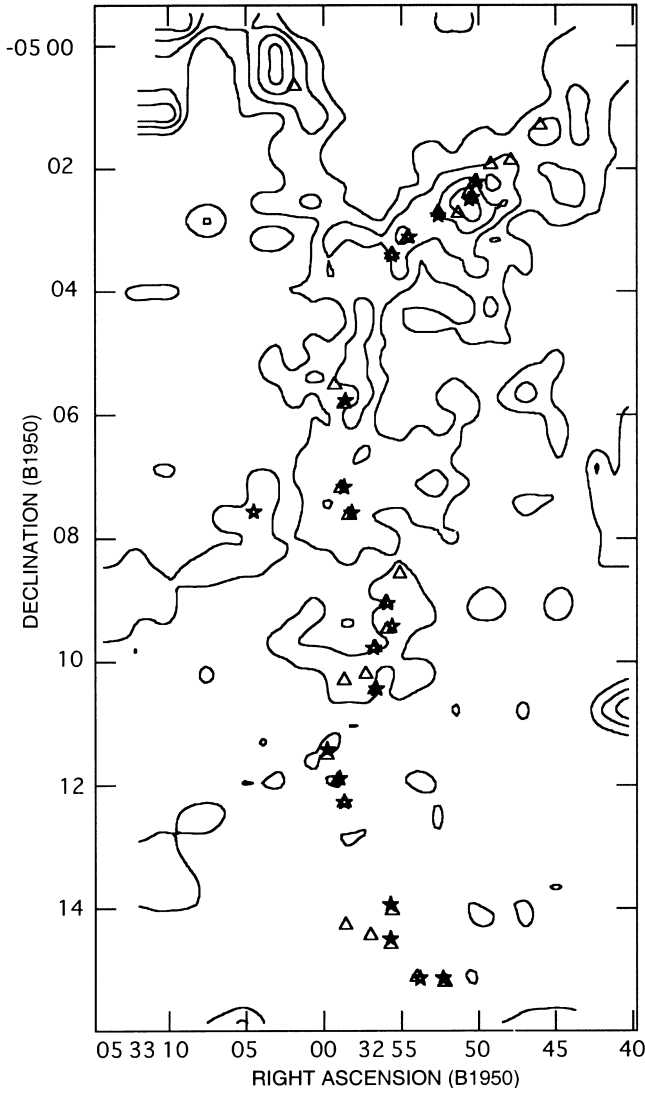


FIG. 7.—Map of the $\text{H}^{13}\text{CO}^+/\text{HCO}^+$ integrated intensity ratio. Contour intervals are 0.1 starting at 0.1.

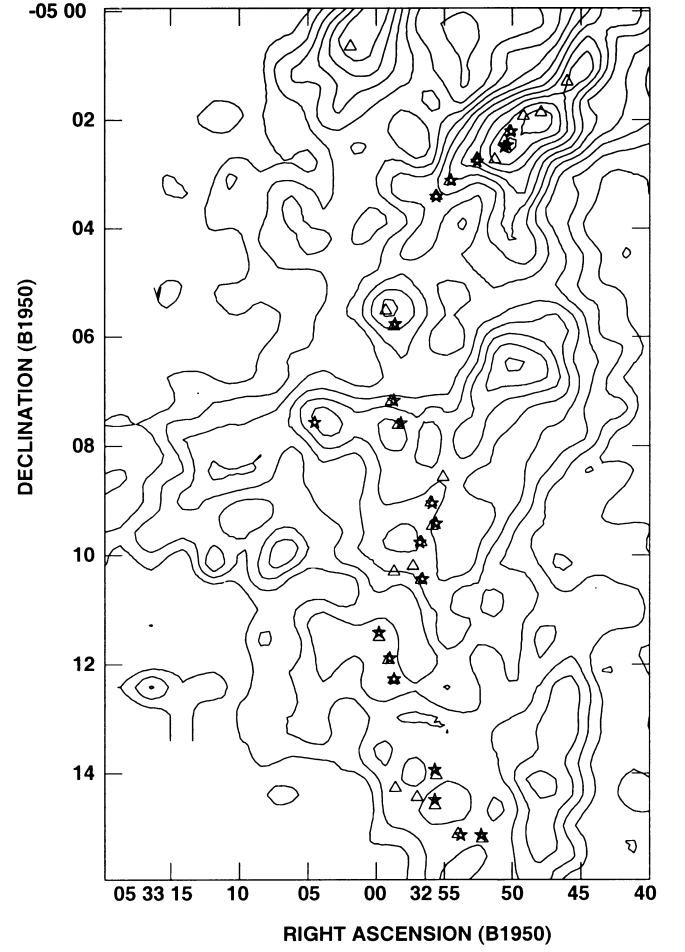


FIG. 8.— $\text{C}^{18}\text{O}(1-0)$ integrated intensity map of the OMC-2/3 region. Contour intervals are 0.44 K km s^{-1} starting at 0.66 K km s^{-1} . The stars mark the 1.3 mm continuum sources (Chini et al. 1997), and the triangles mark the $350 \mu\text{m}$ continuum sources (Lis et al. 1998).

TABLE 10
OUTFLOWS IN DARK CLOUDS AND ORION KL

SOURCE	P_{flow}		M_{core}		ΔV_{inc} (km s^{-1})
	$M_{\odot} \text{ km s}^{-1}$	Reference	M_{\odot}	Reference	
L1455	4.5	1	16	2	0.28
L1489	0.040	3	0.57	4	0.07
L1551	5.3	5	4.6	4	1.2
B35	2.0	3	48	6	0.04
L1535	0.17	7	0.7	8	0.24
L43	0.12	3	2	4	0.06
L723	1.0	1	0.55	9	1.8
B335	0.30	1	2.7	4	0.11
L1172	2.3	3	3.7	4	0.62
Orion KL	160	10	1800	11	0.089

REFERENCES.—(1) Goldsmith et al. 1984; (2) Torrelles et al. 1986; (3) Myers et al. 1988; (4) Myers & Benson 1983; (5) Schloerb & Snell 1984; (6) Benson & Myers 1989; (7) Heyer et al. 1987; (8) Ungerechts, Winnewisser, & Walmsley 1982; (9) Hirano et al. 1998; (10) Snell et al. 1984; (11) Tatematsu et al. 1993.

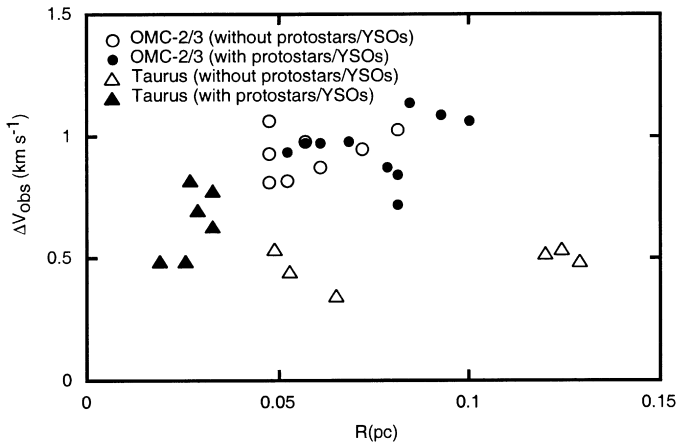


FIG. 9.—Line width-radius (ΔV_{obs} - R) diagram for the H^{13}CO^+ cores. The open circles show OMC-2/3 cores without protostars/YSOs, and the filled circles show OMC-2/3 cores with protostars/YSOs obtained in this work. The open triangles show Taurus cores without protostars/YSOs, and the filled triangles show Taurus cores with protostars/YSOs (Mizuno et al. 1994).

We discuss the dynamical influence of outflows on cores. The line width of the core will increase by $\Delta V_{\text{inc}} = P_{\text{flow}}/M_{\text{core}}$ (km s^{-1}), if all the momentum of the outflow P_{flow} is used for increasing the line width of the core one-dimensionally. As shown in Figure 12, the OMC-2/3 cores have smaller ΔV_{inc} compared with the cores in dark clouds because of larger core masses. These small values of $\Delta V_{\text{inc}} \lesssim 0.1$ (km s^{-1}) in OMC-2/3 hardly alter the line widths of massive cores, which have large line widths intrinsically. Thus, we conclude that the influence of the outflow is negligible in OMC-2/3. In dark clouds, the average ΔV_{inc} is of order 0.3 km s^{-1} . The actual influence of the outflow is

smaller because all the momentum of the outflow is not used for increasing the core line width. In Taurus, the observed difference of the ΔV_{obs} between the cores with YSOs and those without YSOs is $\sim 0.17 \text{ km s}^{-1}$ (Mizuno et al. 1994). The difference in observed ΔV_{obs} , $\sim 0.17 \text{ km s}^{-1}$, corresponds to a difference in ΔV_{tot} of $\sim 0.14 \text{ km s}^{-1}$. After correcting for this value for ΔV_{tot} of dark cloud cores, we plotted the relation between \dot{M}_{flow} and ΔV_{tot} in Figure 13, which gives

$$\log(\dot{M}_{\text{flow}}/M_{\odot} \text{ yr}^{-1}) = (-4.9 \pm 0.1) + (2.9 \pm 0.4) \log(\Delta V_{\text{tot}}/\text{km s}^{-1}). \quad (6)$$

This relation is in good agreement with equation (4). From this, we have a linear form

$$\dot{M}_{\text{flow}} = (0.74^{+0.22}_{-0.17}) \dot{M}_{\text{acc}}. \quad (7)$$

5.2. Efficiency of Momentum Transfer to Outflows

Most of the outflow matter is the ambient gas swept up by a jet/wind, which is thought to originate in the innermost regions of the circumstellar disk around a protostar (e.g., Königl & Ruden 1993). With the efficiency η of the momentum transfer from the ejected jet/wind to the outflow, the mass-loss rate \dot{M}_{flow} can be expressed as

$$\dot{M}_{\text{flow}} = \eta \frac{V_w}{V_{\text{flow}}} \dot{M}_w = \eta \frac{V_w}{V_{\text{flow}}} \frac{\dot{M}_w}{\dot{M}_{\text{acc}}} \dot{M}_{\text{acc}}, \quad (8)$$

where \dot{M}_w and V_w are the mass ejection rate and velocity, respectively, of the jet/wind.

Typically, V_w is several 100 km s^{-1} judging from the velocities of HH objects (Schwartz 1983) and extremely high-velocity (EHV) CO flows (e.g., Bachiller 1996), and

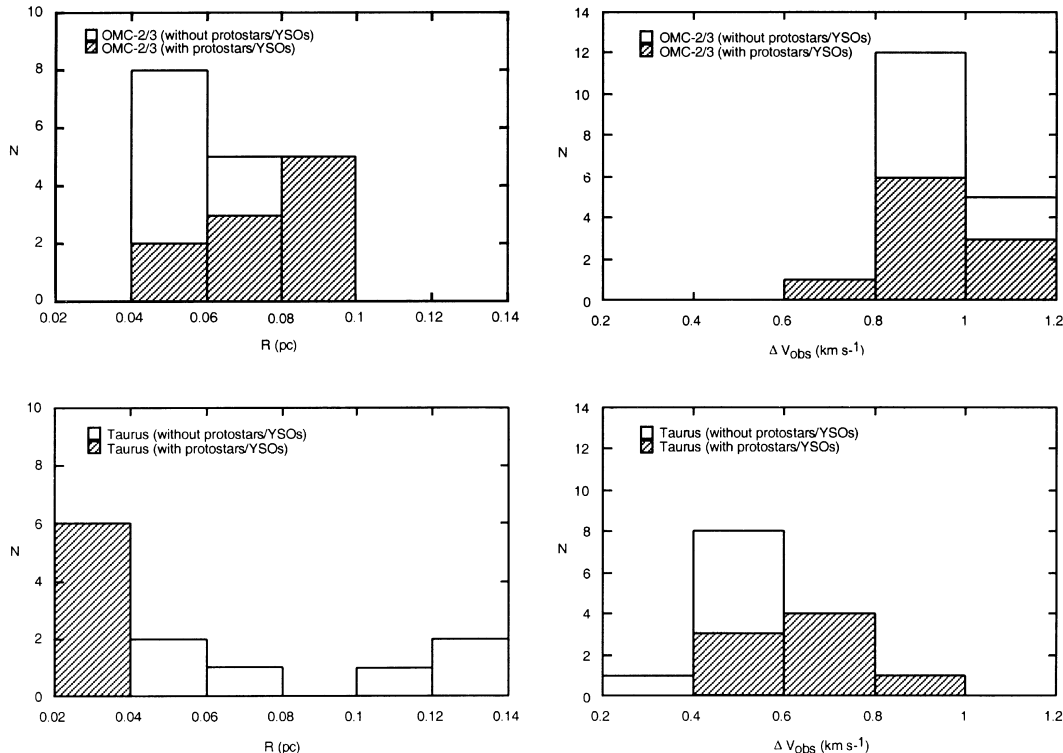


FIG. 10.—Histograms of the radius (R) and the line width (ΔV_{obs}) of the H^{13}CO^+ line of the dense cores in the OMC-2/3 region and Taurus. Shading indicates the cores associated with protostars/YSOs.

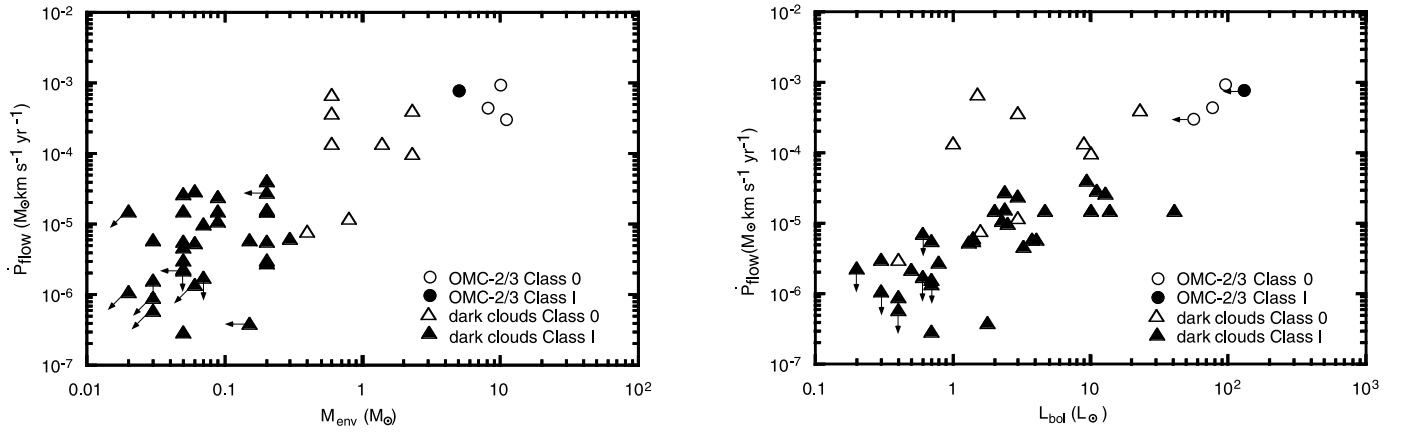


FIG. 11.—*Left*: Momentum flux \dot{P}_{flow} for CO outflows against envelope mass M_{env} . *Right*: \dot{P}_{flow} against bolometric luminosity L_{bol} . The open circles show Class 0 sources, the filled circles show Class I sources in OMC-2/3, the open triangles show Class 0 sources, and the filled triangles show Class I sources in dark clouds (Bontemps et al. 1996).

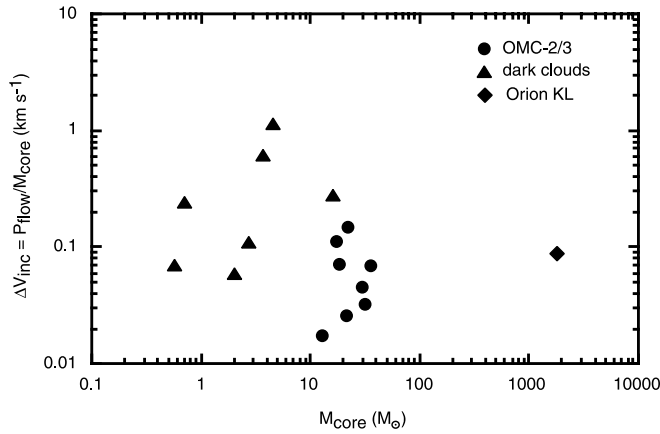


FIG. 12.—Expected maximum dynamical influence of the outflow on the core. The increase of the line width ΔV_{inc} is defined as P_{flow} divided by M_{core} assuming that all of the outflow is converted into the one-dimensional momentum of the core gas. The circles represent the OMC-2/3 sources, triangles represent dark cloud sources, and the diamond represents Orion KL.

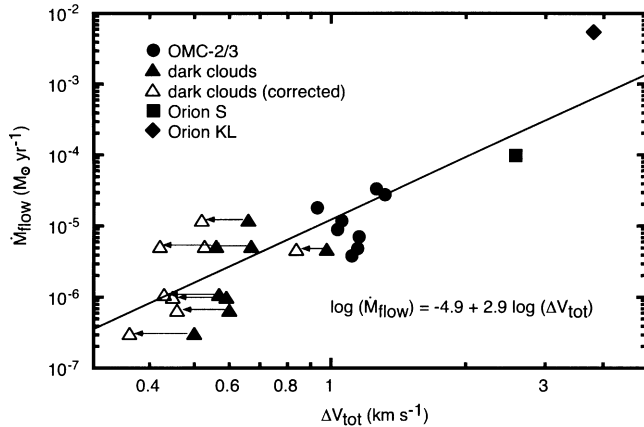


FIG. 13.—Mass-loss rate \dot{M}_{flow} of the CO outflow plotted against the total line width ΔV_{tot} of the core. The circles are the OMC-2/3 sources, the triangles are dark cloud sources, the square is Orion S, and the diamond is Orion KL.

V_{flow} is several 10 km s^{-1} . If $\dot{M}_w/\dot{M}_{\text{acc}} \approx 0.1$, our empirical relation (eq. [7]) suggests the efficiency is of order $\eta \approx 0.7$. For the value of $\dot{M}_w/\dot{M}_{\text{acc}} \approx 0.3$ suggested by Shu et al. (1994), we have smaller η (~ 0.2).

5.3. Physical Properties of the Dense Cores and Comparisons with Theory

We speculate about the factors which initiate star formation. To address this problem, we make clear a difference between dense cores with protostars/YSOs and those without protostars/YSOs.

We compare the observed properties of the dense cores with Nakano's (1998) model. Neglecting the effect of magnetic field and assuming the core to be spherical and uniform for simplicity, the virial equation (eq. [6] of Nakano 1998) reduces to

$$\frac{1}{2} \frac{d^2 I}{dt^2} = 3C_{\text{eff}}^2 M_{\text{core}} - \frac{3}{5} \frac{GM_{\text{core}}^2}{R} - 4\pi R^3 P_s \equiv F(R), \quad (9)$$

where M_{core} , R , and I are the mass, radius, and generalized moment of inertia, respectively, of the core and P_s is the pressure of the surrounding medium. The core is in equilibrium when $F(R) = 0$. For given M_{core} and C_{eff} , there is a critical value P_{cr} for the pressure of the surrounding medium, P_s , above which no equilibrium states exist. Nakano's (1998) equation (27) gives

$$P_{\text{cr}} = \frac{1}{12\pi G^3 M_{\text{core}}^2} \left(\frac{5}{3} \right)^3 \left(\frac{9}{4} C_{\text{eff}}^2 \right)^4. \quad (10)$$

At this critical state $P_s = P_{\text{cr}}$, the core has an equilibrium state with radius

$$R_{\text{cr}} = \frac{4GM_{\text{core}}}{15C_{\text{eff}}^2}. \quad (11)$$

The core begins dynamical contraction when the critical pressure P_{cr} has decreased below the pressure P_s of the surrounding medium by dissipation of turbulence; P_{cr} depends sensitively on the effective sound speed and on the core mass.

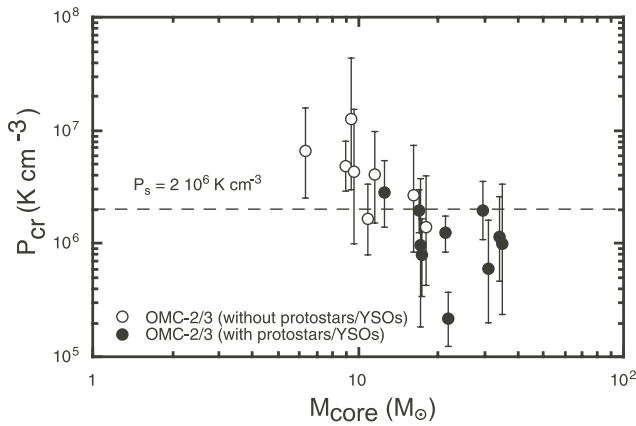


FIG. 14.—Critical surface pressure P_{cr} (eq. [10]) for hydrostatic equilibrium plotted against mass M_{core} for the dense cores in the OMC-2/3 region. The dashed line shows the surface pressure $P_s = 2 \times 10^6 \text{ K cm}^{-3}$ derived for this region. The error bars correspond to the 1σ deviation of the line width within the half-intensity contour of the integrated intensity.

Figure 14 shows the critical pressure P_{cr} against the core mass M_{core} for the OMC-2/3 cores. The cores without protostars/YSOs tend to have larger P_{cr} ($\gtrsim 2 \times 10^6 \text{ K cm}^{-3}$), while the cores with protostars/YSOs tend to have smaller P_{cr} ($\lesssim 2 \times 10^6 \text{ K cm}^{-3}$). The H_2 column density in the ^{13}CO filament in OMC-2/3, in which the observed dense cores are embedded, ranges from about 3×10^{21} to $45 \times 10^{21} \text{ cm}^{-2}$ (Castets et al. 1990). We adopt $N(\text{H}_2) \sim 1.5 \times 10^{22} \text{ cm}^{-2}$ or $A_V \sim 15 \text{ mag}$. A cloud with this column density has a mean pressure $\sim 2 \times 10^6 \text{ K cm}^{-3}$ in equilibrium, according to equation (33) of Nakano (1998), which is mean surface pressure on cores embedded therein. Thus, we suggest that the cores with $P_{\text{cr}} < 2 \times 10^6 \text{ K cm}^{-3}$ ($= P_s$) have already begun dynamical collapse and are forming stars.

Figure 15 plots the virial theorem function $F(R)$ defined by equation (9) for the observed cores against R/R_{cr} . Nakano (1998) assumed that the core is initially in a stable equilibrium state ($F = 0$ and $R/R_{\text{cr}} > 1$). The core contracts gradually reducing R/R_{cr} by dissipation of turbulence. Just after the core reaches the critical point ($F = 0$ and $R/R_{\text{cr}} = 1$), the core begins dynamical collapse because no equilibrium states exist, and finally stars form. The result shown in Figure 15 is consistent with the scenario: the cores without protostars/YSOs are in the equilibrium state ($F = 0$ and $R/R_{\text{cr}} > 1$), while the cores with protostars/YSOs are dynamically collapsing ($F < 0$). The cores with YSOs have smaller R/R_{cr} than the cores without YSOs, although R itself is similar or slightly larger (see Figs. 9 and 10). Because R_{cr} is proportional to M_{core} , cores with YSOs (which have larger mass) have smaller R/R_{cr} , even though R is larger.

As discussed by Nakano (1998), the cores with larger mass begin dynamical collapse in an earlier stage of turbulence dissipation because P_{cr} is proportional to M_{core}^{-2} . The

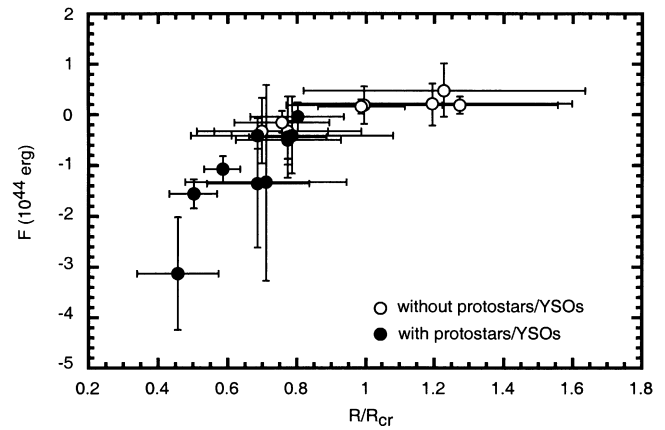


FIG. 15.—Virial theorem function F (eq. [9]) is plotted against the radius R divided by R_{cr} (eq. [11]) for the H^{13}CO^+ cores in the OMC-2/3 region. The error bars correspond to the deviation of the line width within the half-intensity contour of the integrated intensity.

cores with lower mass must dissipate turbulence to higher degrees before they begin dynamical contraction.

6. SUMMARY

We identified 18 dense cores and eight molecular outflows in the OMC-2/3 region. Ten of these cores are accompanied by protostars/YSOs. The following characteristics are found for the cores and the outflows.

1. The H^{13}CO^+ line emission of the cores is optically thicker in OMC-3 than in OMC-2. This probably reflects the younger evolutionary stage of OMC-3.
2. The line widths of the H^{13}CO^+ cores in OMC-2/3 are twice as large as those in dark clouds, and the momentum fluxes of the outflows in OMC-2/3 are approximately 2 orders of magnitude larger than those in dark clouds.
3. The mass-loss rate of the outflow is proportional to the third power of the core line width, indicating that the mass-loss rate is proportional to the mass accretion rate onto the protostar.
4. The outflows have negligible dynamical influence on the line widths of the cores in OMC-2/3, while in dark clouds outflows have some dynamical influence on dense cores.
5. The observed characteristics of the cores are consistent with the model of star formation developed by Nakano (1998), in which dynamical contraction sets in by (partial) dissipation of turbulence.

We thank Munetake Momose for comments on the draft. This work was partly supported by a Research Fellowship of the Japan Society for the Promotion of Science for Young Scientists (11-10299) and a Grant-in-Aid for Scientific Research of the Japan Society for the Promotion of Science (11440067).

APPENDIX A

INDIVIDUAL OUTFLOWS

A1. CSO 2, MMS 2–4, AND MMS 5

An outflow associated with CSO 2 is clear in HCO^+ (Fig. 16a) but not clear in CO.

Chini et al. (1997) reported that MMS 6 is surrounded by the redshifted gas. We regard this red lobe at ($5^{\text{h}}32^{\text{m}}56^{\text{s}}$, $-5^{\circ}3'30''$) and the blue lobe at ($5^{\text{h}}32^{\text{m}}49^{\text{s}}$, $-5^{\circ}3'30''$) as being associated with MMS 5 judging from the axis of the H_2 jet (Figs. 16b and 16c). Another blue lobe ($5^{\text{h}}32^{\text{m}}56^{\text{s}}$, $-5^{\circ}2'30''$) is associated with core AC3. However, it is not clear which of the protostars MMS 2–4 in AC3 is accompanied by this outflow. In this outflow, the HCO^+ distribution of the blue lobe and the H_2 knot (northeast side of MMS 4) is well correlated. Emission from the red lobe is not detected in either CO or HCO^+ .

A2. MMS 7

In CO, the red lobe is well collimated but the blue lobe is not collimated (Fig. 16d). The blue lobe is weaker than the red lobe. MMS 7 is located along the axis of the red lobe. A bipolar outflow is not clearly seen in HCO^+ .

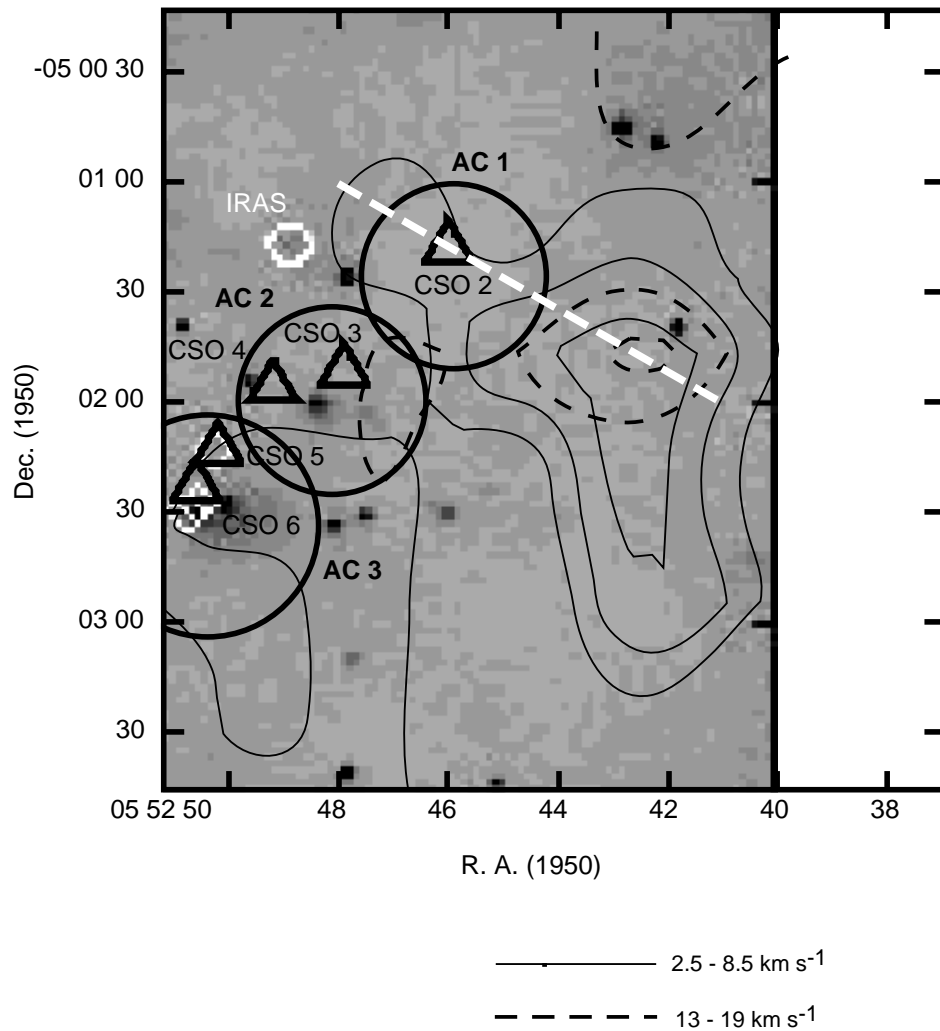


FIG. 16a

FIG. 16.—Maps of the outflows superimposed on images of H_2 emission (Yu et al. 1997). The solid line represents the distribution of the blue lobe, and the dashed line represents the red lobe. (a) CSO 2 in the HCO^+ line. The lowest contour and contour intervals are 0.35 and 0.2 K km s^{-1} . (b) MMS 2–4 and MMS 5 in the CO line. The lowest contour and contour intervals are 3 and 2 K km s^{-1} . (c) MMS 2–4 and MMS 5 in the HCO^+ line. The lowest contour and contour intervals are 0.5 and 0.1 K km s^{-1} for the blue lobe and 0.3 and 0.1 K km s^{-1} for the red lobe. (d) MMS 7 in the CO line. The lowest contour and contour intervals are 2 and 1 K km s^{-1} for the blue lobe and 3 and 2 K km s^{-1} for the red lobe. (e) MMS 9 in the CO line. The lowest contour and contour intervals are 3 and 3 K km s^{-1} . (f) MMS 9 in the HCO^+ line. The lowest contour and contour intervals are 0.7 and 0.4 K km s^{-1} . (g) MMS 10 in the CO line. The lowest contour and contour intervals are 4 and 4 K km s^{-1} . (h) MMS 10 in the HCO^+ line. The lowest contour and contour intervals are 0.8 and 0.2 K km s^{-1} . (i) FIR 1 in the CO line. The lowest contour and contour intervals are 2 and 2 K km s^{-1} . (j) FIR 1 in the HCO^+ line. The lowest contour and contour intervals are 0.6 and 0.2 K km s^{-1} . (k) OMC-2 in the CO line. The lowest contour and contour intervals are 3 and 2 K km s^{-1} . (l) OMC-2 in the HCO^+ line. The lowest contour and contour intervals are 1 and 0.2 K km s^{-1} . (m) The integrated intensity ratio (HCO^+/CO) in OMC-2. The lowest contour and contour intervals are 0.2 and 0.1 K km s^{-1} .

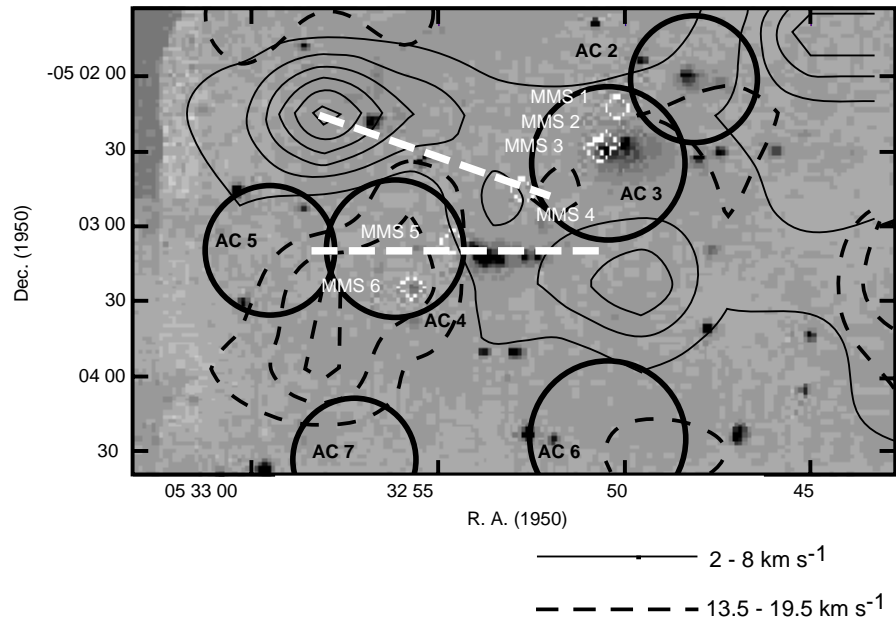


FIG. 16b

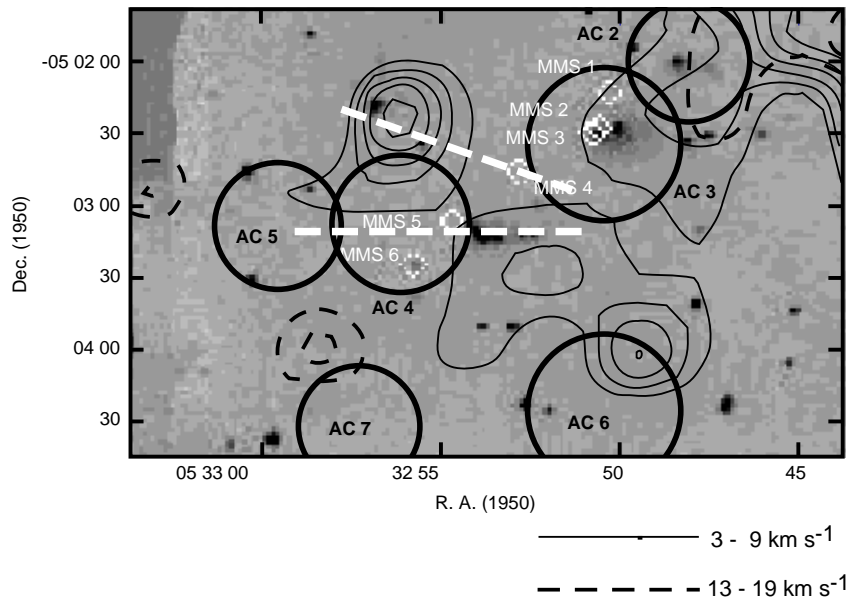


FIG. 16c

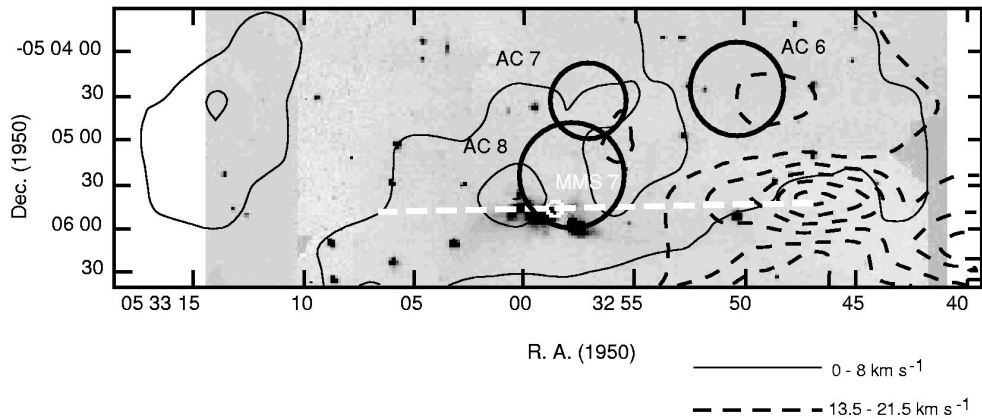


FIG. 16d

A3. MMS 9 AND MMS 10

We identified an outflow from MMS 9 (Figs. 16e and 16f). Chini et al. (1997) regarded the same outflow as being associated with MMS 8. However, because the CO/HCO⁺ outflows in our observations show good correlation with the H₂ jet and also because H₂O maser (Cesaroni et al. 1988) is associated with MMS 9, it seems less likely that this outflow is driven by MMS 8. Reipurth et al. (1999) detected 3.6 cm continuum source toward MMS 9, but not toward MMS 8, which might support our interpretation. MMS 10 seems to be accompanied by a blue lobe, though the red lobe is difficult to identify because it seems to be overlapped with that of MMS 9 (Figs. 16g and 16h).

A4. FIR 1

We identified blue and red lobes associated with FIR 1, but it is not clear which of the sources FIR 1a–1c is associated with this outflow (Figs. 16i and 16j). The blue lobe is confused with the outflow associated with MMS 9.

A5. OMC-2

The blue and red lobe overlap each other (Figs. 16k and 16l). Unlike the CO outflow, the HCO⁺ outflow is elongated and well correlated with the axis of the H₂ jet. The integrated intensity ratio of HCO⁺/CO of the wing emission tends to be larger

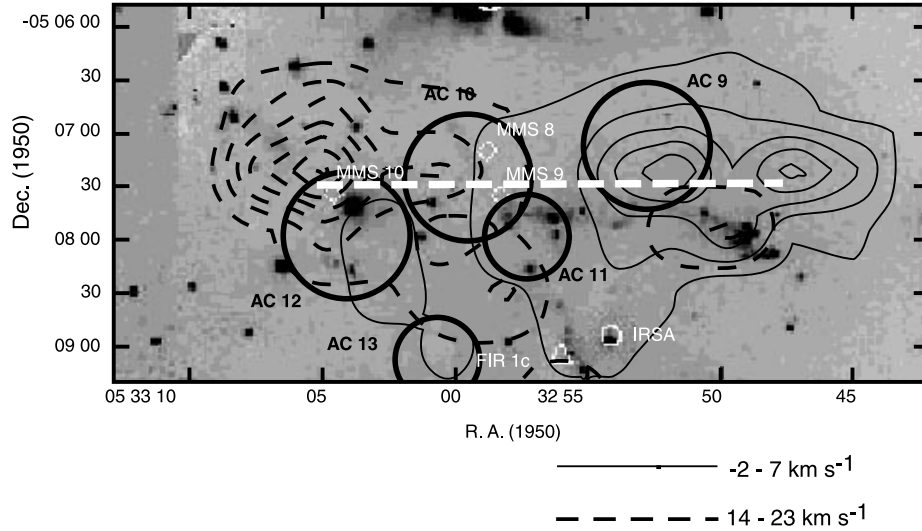


FIG. 16e

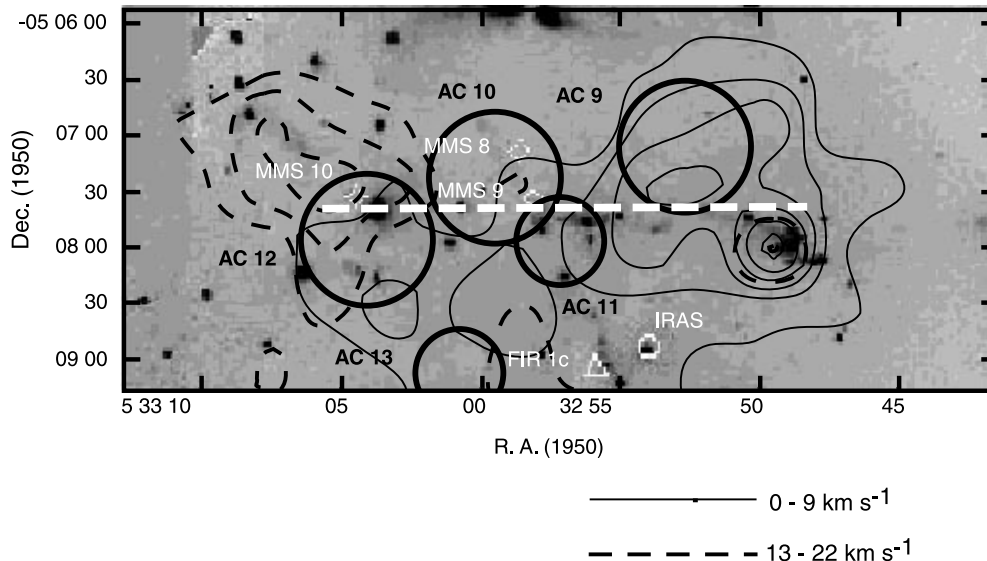
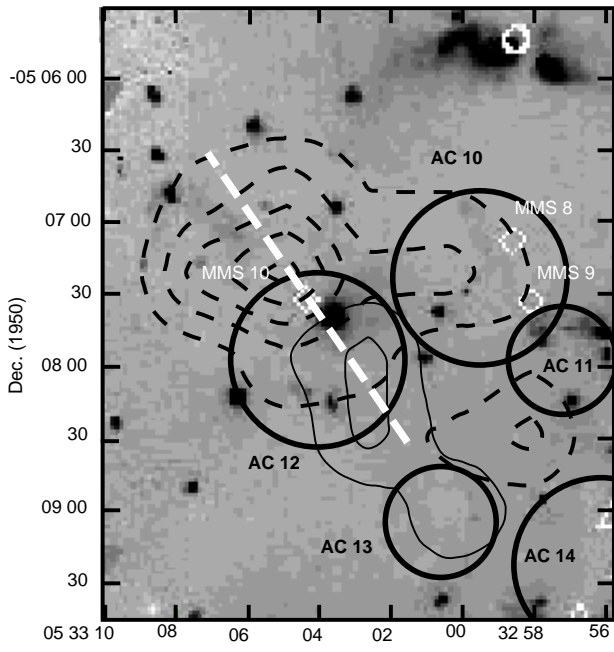
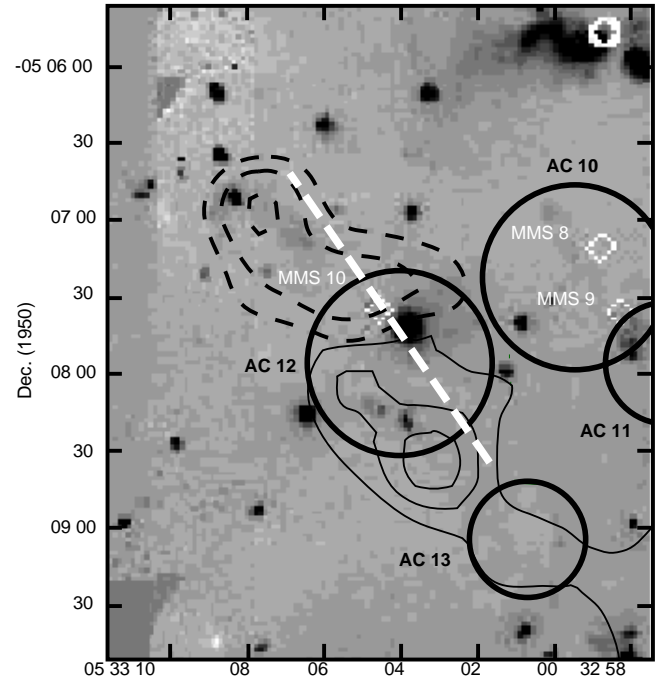


FIG. 16f



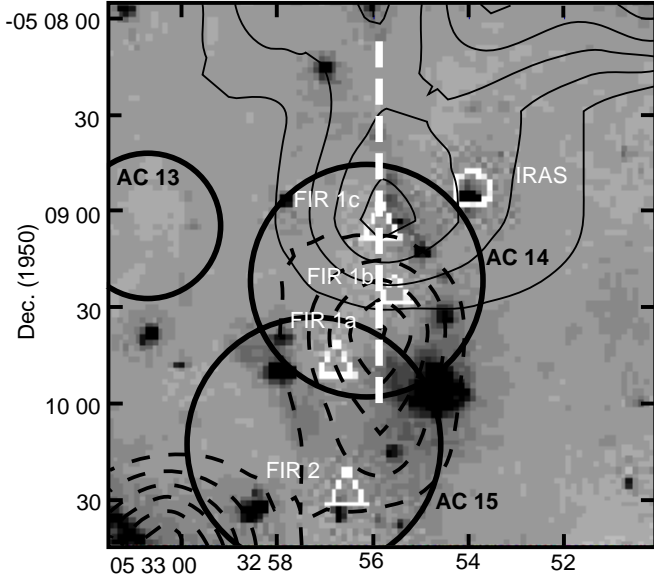
— 0 - 8 km s⁻¹
 - - - 11 - 22 km s⁻¹

FIG. 16g



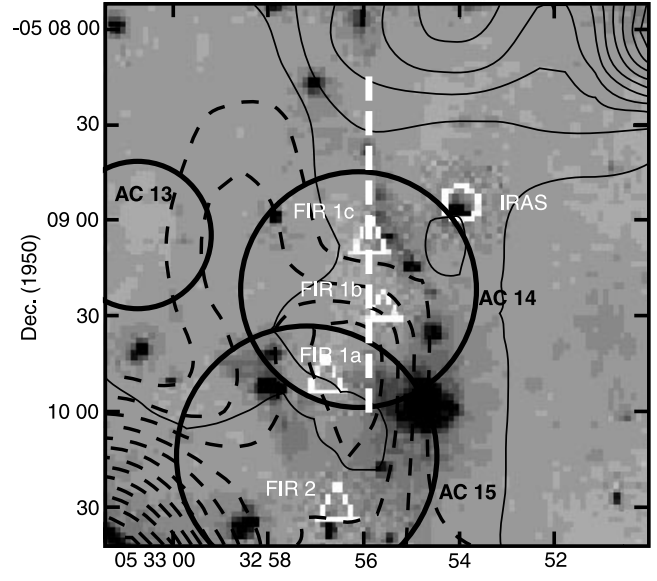
— 0 - 9 km s⁻¹
 - - - 14 - 23 km s⁻¹

FIG. 16h



— 0 - 8 km s⁻¹
 - - - 14 - 22 km s⁻¹

FIG. 16i



— -0.5 - 8.5 km s⁻¹
 - - - 13 - 22 km s⁻¹

FIG. 16j

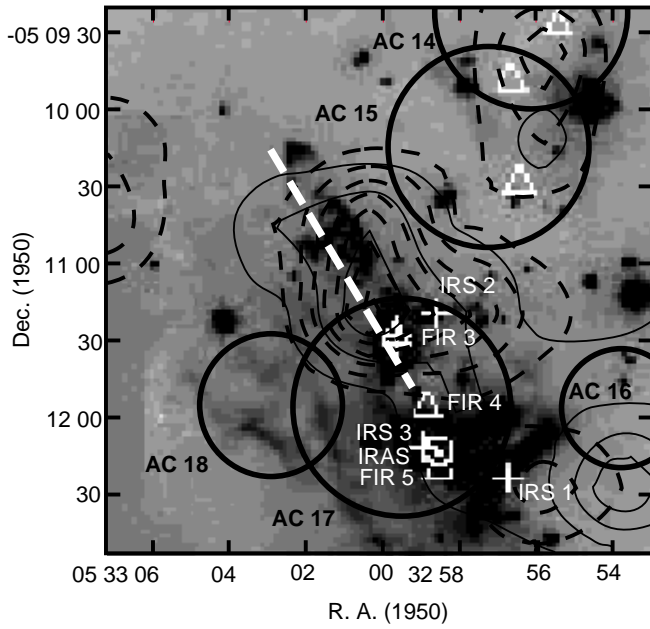


FIG. 16k

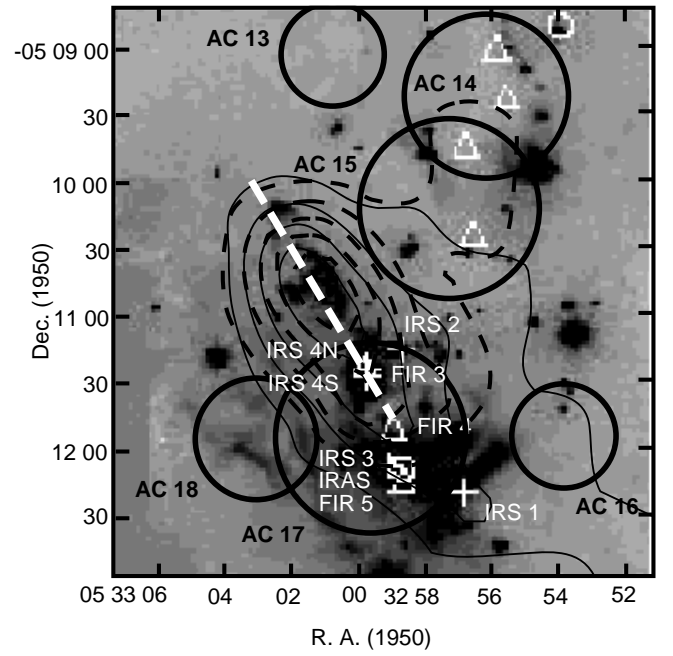


FIG. 16l

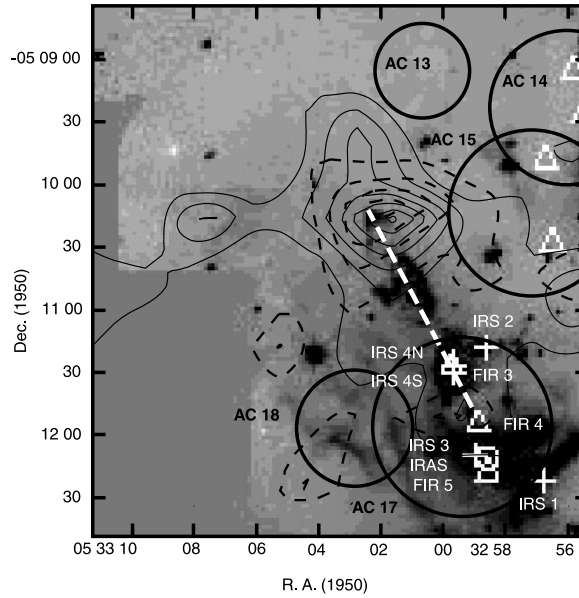


FIG. 16m

at the front end of the H_2 jet (Fig. 16m). We have also found this tendency in MMS 2–4 and MMS 9. The abundance of HCO^+ may have been enhanced there due to the shock chemistry of the jet (cf. Hasegawa & Mitchell 1995).

A6. COMPARISON OF THE CO OUTFLOWS WITH THE HCO^+ OUTFLOWS

In general, the CO and HCO^+ outflows show similar distribution. However, some outflows show different distributions between CO and HCO^+ (e.g., OMC-2). The CSO 2 outflow is clear in HCO^+ but not clear in CO. Toward H_2 knots (Yu et al. 1997), both the CO and HCO^+ outflows tend to have stronger integrated intensities and larger velocity widths. This tendency is more clearly seen in HCO^+ . In many cases, H_2 knots accompany only blue lobes of CO/ HCO^+ outflows. This is probably because the H_2 emission from the red lobe is absorbed by the dust surrounding the protostar.

REFERENCES

- André, P., Ward-Thompson, D., & Barsony, M. 1993, *ApJ*, 406, 122
- Bachiller, R. 1996, *ARA&A*, 34, 111
- Bachiller, R., Martin-Pintado, J., & Planesas, P. 1991, *A&A*, 251, 639
- Batra, W., Wilson, T. L., Bastien, P., & Ruf, K. 1983, *A&A*, 128, 279
- Benson, P. J., & Myers, P. C. 1980, *ApJ*, 242, L87
- . 1989, *ApJS*, 71, 89
- Bontemps, S., André, P., Terebey, S., & Cabrit, S. 1996, *A&A*, 294, 835
- Castets, A., Duvert, G., Dutrey, A., Bally, J., Langer, W. D., & Wilson, R. W. 1990, *A&A*, 234, 469
- Castets, A., & Langer, W. D. 1995, *A&A*, 294, 835
- Cesaroni, R., Palagi, F., Felli, E., Catarzi, M., Comoretto, G., Di Franco, S., Giovanardi, C., & Palla, F. 1988, *A&AS*, 76, 445
- Cesaroni, R., & Wilson, T. L. 1994, *A&A*, 281, 209
- Chini, R., Reipurth, B., Ward-Thompson, D., Bally, J., Nyman, L.-Å., Sievers, A., & Billawala, Y. 1997, *ApJ*, 474, L135
- Edwards, S., Ray, T., & Mundt, R. 1993, in *Protostars and Planets III*, ed. E. H. Levy & J. I. Lunine (Tucson: Univ. Arizona Press), 567
- Fischer, J., Sanders, D. B., Simon, M., & Solomon, P. M. 1985, *ApJ*, 293, 508
- Fukui, Y., Iwata, T., Mizuno, A., & Bally, J. 1993, in *Protostars and Planets III*, ed. E. H. Levy & J. I. Lunine (Tucson: Univ. Arizona Press), 603
- Goldsmith, P. F., Snell, R., & Heyer, M. H. 1984, *ApJ*, 286, 599
- Harju, J., Walmsley, C. M., & Wouterloot, J. G. A. 1991, *A&A*, 245, 643
- Hasegawa, T. I., & Mitchell, G. F. 1995, *ApJ*, 441, 665
- Herbig, G. H., & Bell, K. R. 1988, *Third Catalog of Emission-Line Stars of the Orion Population* (Santa Cruz: Lick Obs.)
- Heyer, M. H., Snell, R. L., Goldsmith, P. F., & Myers, P. C. 1987, *ApJ*, 321, 370
- Hirano, N., Hayashi, S., Umemoto, T., & Ukita, N. 1998, *ApJ*, 504, 334
- Johnson, J. J., Gehr, R. D., Jones, T. J., Hackwell, J. A., & Grasdalen, G. L. 1990, *AJ*, 100, 518
- Johnstone, D., & Bally, J. 1999, *ApJ*, 510, L49
- Königl, A., & Ruden, S. P. 1993, in *Protostars and Planets III*, ed. E. H. Levy & J. I. Lunine (Tucson: Univ. Arizona Press), 641
- Larson, R. B. 1982, *MNRAS*, 200, 159
- Lee, H. H., Bettens, R. P. A., & Herbst, E. 1996, *A&AS*, 119, 111
- Lis, D. C., Serabyn, E., Dowell, C. D., Benford, D. J., Phillips, T. G., Hunter, T. R., & Wang, N. 1998, *ApJ*, 509, 299
- MacLaren, I., Richardson, K. M., & Wolfendale, A. W. 1988, *ApJ*, 333, 821
- Mizuno, A., Onishi, T., Hayashi, M., Ohashi, N., Sunada, K., Hasegawa, T., & Fukui, Y. 1994, *Nature*, 368, 719
- Myers, P. C., & Benson, P. J. 1983, *ApJ*, 266, 309
- Myers, P. C., Heyer, M., Snell, R. L., & Goldsmith, P. F. 1988, *ApJ*, 324, 907
- Nakano, T. 1998, *ApJ*, 494, 587
- Reipurth, B., Rodriguez, L. F., & Chini, R. 1999, *AJ*, 118, 983
- Schloerb, P., & Snell, R. 1984, *ApJ*, 283, 129
- Schmid-Burgk, J., Güsten, R., Mauersberger, R., Schulz, A., & Wilson, T. L. 1990, *ApJ*, 362, L25
- Schwartz, R. D. 1983, *ARA&A*, 21, 209
- Shu, F. H. 1977, *ApJ*, 214, 488
- Shu, F. H., Lizano, S., Ruden, S. P., & Najita, J. 1988, *ApJ*, 328, L19
- Shu, F. H., Najita, J., Ostriker, E., Wilkin, F., Ruden, S., & Lizano, S. 1994, *ApJ*, 429, 781
- Snell, R. L., Loren, R. B., & Plambeck, R. L. 1980, *ApJ*, 239, L17
- Snell, R. L., Scoville, N. Z., Sanders, D. B., & Erickson, N. R. 1984, *ApJ*, 284, 176
- Sunada, K., Noguchi, T., Tsuboi, M., & Inatani, J. 1995, in *ASP Conf. Ser. 75, Multifield Systems for Radio Telescopes*, ed. D. T. Emerson & J. M. Payne (San Francisco: ASP), 230
- Tatematsu, K., et al. 1993, *ApJ*, 404, 643
- Torrelles, J., Ho, P., Moran, J., Rodriguez, L., & Cantó, J. 1986, *ApJ*, 307, 787
- Ungerechts, H., Winnewisser, G., & Walmsley, M. 1982, *A&A*, 111, 339
- Wilson, T. L., Mauersberger, R., Gensheimer, P. D., Muders, D., & Bieging, J. H. 1999, *ApJ*, 525, 343
- Yu, K. C., Bally, J., & Devine, D. 1997, *ApJ*, 485, L45